Robotica: (2020) volume 38, pp. 1041–1063. © Cambridge University Press 2019
doi:10.1017/S0263574719001243

Optimal Feet-Forces' and Torque Distributions of Six-Legged Robot Maneuvering on Various Terrains

Abhijit Mahapatra†, Shibendu Shekhar Roy‡ and Dilip Kumar Pratihar¶*

†*Advanced Design and Analysis Group, CSIR-Central Mechanical Engineering Research Institute, Durgapur 713209, India*
‡*Department of Mechanical Engineering, National Institute of Technology, Durgapur 713209, India*
¶*Department of Mechanical Engineering, Indian Institute of Technology, Kharagpur 721302, India*

(Accepted July 18, 2019. First published online: August 15, 2019)

SUMMARY
An analytical model with coupled dynamics for a realistic six-legged robotic system locomoting on various terrains has been developed, and its effectiveness has been proven through computer simulations and validated using virtual prototyping tools and real experiment. The approach is new and has not been attempted before. This study investigated the optimal feet-forces' distributions under body force and foot–ground interaction considering compliant contact and friction force models for the feet undergoing slip. The kinematic model with 114 implicit constraints in 3D Cartesian space has been transformed in terms of generalized coordinates with a reduced explicit set of 24 constrained equations using kinematic transformations. The nonlinear constrained inverse dynamics model of the system has been formulated as a coupled dynamical problem using Newton–Euler method with realistic environmental conditions (compliant foot–ground contact, impact, and friction) and computed using optimization techniques due to its indeterminate nature. One case study has been carried out to validate the analytical data with the simulated ones executed in MSC.ADAMS® (Automated Dynamic Analysis of Mechanical Systems), while the other case study has been conducted to validate the analytical and simulated data with the experimental ones. In both these cases, results are found to be in close agreement, which proves the efficacy of the model.

KEYWORDS: Six-legged robot; Coupled multibody dynamics; Foot–terrain interactions; Optimal feet-forces; Quadratic programming.

1. Introduction

A lot of studies had been carried out by researchers worldwide related to the kinematics, dynamics, and control of six-legged robots.[1–3] Most of those studies were simplified to avoid the complexities involved in the robot dynamics of six-legged robots. In addition to that, the model capabilities were limited to the study of kinematics and dynamics of the system locomoting on flat terrain,[3,4] though very few simplified models in the recent past were developed for locomotion on uneven terrain.[5] Furthermore, the studies were conducted based on single leg dynamics or trunk body and legs as separate entities, or in some cases the effects of mass and inertia of legs had been neglected.[6–8] Moreover, the models neglected the coupling effects and nonlinearity in the dynamics of the swing legs on the support legs and trunk body. These approaches could not depict the real dynamics of the legged robotic system.

* Corresponding author. E-mail: dkpra@mech.iitkgp.ac.in

Furthermore, to evaluate the system's performance, modeling of the interaction mechanics between contacting bodies for multi-body dynamic simulations is important. The models must take into account the events like impact[9] and frictional contact mechanics[10] of leg-tip in contact with the ground for successful design and optimization of the dynamic parameters (i.e., forces, torques, etc.). Both the events couple the normal and tangential (a discontinuous function of sliding velocity and independent of tangential displacement) contact forces, thereby playing a fundamental role in the design, performance analysis, multibody dynamic simulations, and control of legged robots. It is also important to note that whenever a leg-tip touches the ground with a nonzero velocity, impact phenomenon occurs. This phenomenon defines the transition between the swing motion of the legs and contact state characteristics, thereby imposing kinematic constraints on the foot.[11] Gradually, the impact transforms into a frictional contact force problem[12,13] with a slippage of the leg-tip on the terrain. Such contact models can be classified into two types, namely rigid and compliant. Most of the previous models dealing with contact force distribution in legged robots considered the phenomenon as a rigid-body point contact (only force components) without impact and any slippage, thereby not analyzing the actual contact under each foot.[4,6,14–16] However, it is to be noted that rigid-body point contact fails to capture the full range of contact phenomena like the deformation between contacting bodies. In such cases, compliant contact force models are essential.[17,18] Hence, a few researchers considered the leg as a compliant multi-articular structure.[19–21] A few other investigators[22,23] considered compliant leg-tip and studied explicitly the normal contact force models, which were expressed as the functions of local position along the normal and its rate of change. This compliance in the model at the interaction zone between foot and ground is necessary to absorb the unexpected impacts. Such compliant contact phenomenon was first successfully described with a nonlinear spring damper viscoelastic model at the contact point of a sphere and the ground by Hunt and Crossley.[24] This model is well known and is generally called the compliant normal contact force model, which had also been described in the studies of various researchers.[25–30]

Besides the compliant normal contact force, there is also lateral or tangential contact force (also called friction force), which appears during contact as mentioned above. Simple classical Coulomb's (or Amonton's) model[31] is the most widely employed friction force model although it had been modified by various researchers from time to time to tackle their problem of interest like the Dahl's model, Lugre's model, Lueven model, GMS model, Iwan model, etc.[32] Commercially available numerical solver package like MSC.ADAMS® also implements the Coulomb's friction model for realistic dynamic simulation of multi-body systems. However, its mathematical properties complicate the dynamic simulation for both the constrained rigid body dynamics and compliant contact models. Upon the interaction of a foot with a deformable terrain, three contact forces and three contact moments are generated due to deformation of the contact area unlike hard point contact, where only three contact force components are generated. Though a few studies illustrated the idea of contact moment,[26] its effects on the dynamics of the legged system had been neglected.

Furthermore, a legged robotic system is a highly redundant one, that is, infinite number of solutions exist for the interactive forces and moments in a constrained inverse dynamics problem subjected to additional contact constraints. Such redundancy was resolved using optimization methodologies. The objectives were achieved using optimization methods like linear programming (LP) method,[33,34] compact-dual LP (CDLP) method,[35] quadratic programming (QP),[6,15,36,37] pseudo inverse,[17,38] and analytical methods.[39–41] Those methods had been evaluated to find the optimal solution for force distribution and subsequently a real-time implementation on the development of control algorithms for legged robots.

A previous study by Mahapatra *et al*.[42] tackled the coupled dynamic problem, whereby the coupling effect of the swing legs on support legs was addressed. However, the validation of such dynamic model using virtual prototyping (VP) tools and experiments is very much essential. The present study deals with the validation of the developed model[42] (both experimentally and MSC ADAMS simulation) on a six-legged robot either maneuvering on flat terrains or climbing a staircase, prescribing swing leg trajectory in 3D Cartesian space and tackling the coupled multi-body dynamics. In addition to validation, the present study examines the accuracy with which a nonlinear, constrained inverse dynamical model of the six-legged robot could consider the coupling effects of swing legs on the support legs and trunk body, and with which a proposed 3D foot–ground interaction mechanics model (deformable foot on hard terrain with little deformation) could represent compliance between the foot and ground during locomotion on staircase or flat terrains. Also, the dynamic model has been further

https://doi.org/10.1017/S0263574719001243 Published online by Cambridge University Press

improved in the present study by incorporating the calculation of moment arm for the determination of moment at foot-tip. The previous study by Mahapatra *et al.*[42] assumed the moment arm to be equal to zero in the case studies. Furthermore, it is to be noted that although the basic equations are the same as that of Mahapatra *et al.,*[42] in the present study, the terrains are different, and therefore, there are significant changes in the formulation and boundary conditions. The study employed the recursive Newton–Euler (NE) approach to tackle the dynamics of the system without neglecting the inertia and masses of the legs. Furthermore, the objective of minimizing the sum of the squares of joint torques of this coupled dynamical system is mathematically expressed as a constrained optimization problem and solved in MATLAB using QP approach to determine the optimal contact forces' and moments' distributions in all the legs. These obtained solutions of the analytical model have been compared with that of numerical simulations executed in MSC.ADAMS® solver (a commercially available rigid multi-body dynamics numerical solver) and experimental findings. To the best of the authors' knowledge, no such study on six-legged robot's locomotion on various terrains has been reported in the literature, till date.

The paper is organized as follows: Section 2 deals with the dynamic modeling of a six-legged robot. It further discusses the kinematic transformations used to transform the constrained dynamics model from Cartesian coordinates to generalized coordinates. It also presents the contact force interaction mechanics model. Thereafter, it is followed by a constrained optimization framework to minimize the sum of the squares of joint torques in Section 3. Case studies with simulation results and validation are presented in Section 4 followed by a logical conclusion in Section 5.

2. Analytical Modeling of a Six-Legged Robot

The present study deals with the analytical modeling of realistic six-legged robot. A generalized approach is adopted, which will be applicable to any other legged robot design. The multi-legged robotic system forms both close and open chain kinematic loops making it a complex mechanical system. When the legs are connected to one another through a trunk body and also through the ground, it forms a closed chain kinematics loop and the legs are said to be in support phase. Likewise, for an open chain kinematics loop, one of the legs is in swing phase and others are connected to one another only through the trunk body. Forces and moments propagate through these kinematic chains from one leg to another, and therefore, dynamic coupling exists. Kinematic and dynamics equations of motion of such a complex mechanism of the six-legged robotic system maneuvering in various terrains are described in the following sections by taking into consideration multiple reference systems attached to it in Cartesian coordinates (both global and local) and the following assumptions:

1. Trunk body height of the robot can vary during locomotion.
2. Motion of the trunk body, swing legs, slip of support leg's tip, and the Coulomb's friction model (stiction to transition velocity and *vice versa* corresponding to static and dynamic coefficients of friction, respectively) are governed by cubic polynomials.
3. The leg-tip contact area and deformation are small, that is, feet of the robot are not placed in slippery terrain.
4. The magnitude of slip is small in the horizontal plane of the local frame of reference, that is, the robot maneuvers in normal terrain conditions and there is phenomenon of slip, whose magnitude has been assumed in the range of up to 2 mm for the maximum stroke length of 150 mm.
5. Frictionless legged joints.
6. No rebound is considered on impact.

2.1. Reference systems and structure of the robot

Figure 1 displays the Computer Aided Design (CAD) model of an axisymmetric realistic six-legged robot. The main components of the system consist of a central trunk body, six legs, and payload. Each leg has three links that are interconnected to each other and the trunk body through rotary joints, which are independently controlled by three actuators.

The legged system has been modeled as a tree structure[43] with variable architecture, that is, the system has both closed-loop (formed by support legs) and open-chain (formed by swing legs) architecture with respect to the trunk body. To make the formulation generic, two reference frames are

https://doi.org/10.1017/S0263574719001243 Published online by Cambridge University Press

Table I. System parameters.

Parameters		**Values**						
(*I* = 1–6)		**Trunk body**	**Payload**	**Link *i*1**	**Link *i*2**	**Link *i*3**	**Parameters**	**Values**
Mass (kg)		0.650	4.244	0.150	0.041	0.110	e	2.2
	J_{xx}	0.01665	0.009	7.1E-5	2.0E-5	9.80E-5	K	1.0e + 8N/m
Mass	J_{yy}	0.00252	0.003	10.8E-5	8.7E-5	8.70E-5	C_{max}	10e + 6 N/m/s
moment	J_{zz}	0.01690	0.011	5.7E-5	10.0E-5	2.08E-5	p	1.0e - 5 m
of inertia	J_{xy}	0	0	−3.50E-6	12.9E-6	1.23E-10	μ_s	0.3
(kg-m^2)	J_{yz}	0	0	−2.18E-6	1E-6	1.73E-6	μ_d	0.1
	J_{zx}	0	0	−4.96E-6	−7.1E-6	−1.95E-11	v_s	0.01m/s
Effective dimension (m)		0.495 × 0.205 × 0.09	0.150 × 0.09 × 0.04	0.085	0.120	0.100	v_d	0.1m/s

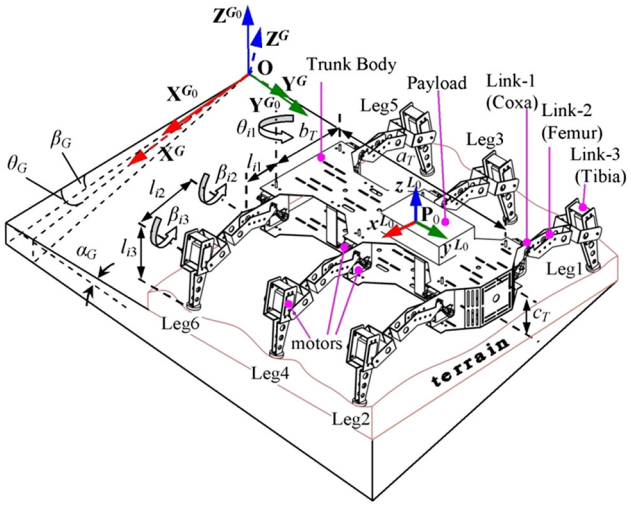

Fig. 1. CAD model of a realistic six-legged robot.

associated with the system: (1) Static Global reference frame $\boldsymbol{G}_0$ and (2) Dynamic reference frame $\boldsymbol{G}$ with respect to XYZ coordinate system. The frames are chosen in such a way that $\boldsymbol{G}$ is the working frame of reference and $\boldsymbol{G}_0$ is fixed frame of reference, which defines the topography (slope, elevation, etc.) and coincide at an arbitrarily chosen origin **O**, whose positional coordinates in the 3D Cartesian frame are defined by (0, 0, 0). A body fixed frame $\boldsymbol{L}_0$ with origin at an arbitrarily chosen point $\mathbf{P}_0$ is assigned to the trunk body. Local frames are attached to joint *ij* (*i* = 1–6 are the leg numbers, *j* = 1–3 are the joint numbers). All the bodies in the system are assumed to be rigid with the joint variables of each leg as θ_{i1}-β_{i2}-β_{i3} corresponding to local axes configurations of joint *ij* respectively. The orientation vectors of Bryant angles[44] are as follows: (1) $\boldsymbol{\eta}_G = [\alpha_G\ \beta_G\ \vartheta_G]^T$ between $\boldsymbol{G}$ and $\boldsymbol{G}_0$ and (2) $\boldsymbol{\eta}_0 = [\alpha_0\ \beta_0\ \vartheta_0]^T$ between $\boldsymbol{L}_0$ and $\boldsymbol{G}$. For details of α_G, β_G, ϑ_G, α_0, β_0, ϑ_0, one may refer to Mahapatra *et al*.[45] It is to be noted that the position of point $\mathbf{P}_0$ on the trunk body with respect to frame $\boldsymbol{G}$ (say, $\mathbf{r}^{G}_{P_0 O}$) can be transformed with respect to frame $\boldsymbol{G}_0$ (say, $\mathbf{r}^{G_0}_{P_0 O}$) using the transformation matrix $\mathbf{A}^{G_0 G}$ that depends on the orientation vector $\boldsymbol{\eta}_G$ between frame $\boldsymbol{G}$ and $\boldsymbol{G}_0$. The values of mass, moment of inertia, and positions of center of mass (COM) of the said realistic robot have been computed using CAD software and are given in Table I.

2.1.1. Constraints equations. To develop the overall kinematics model of the robotic system, it is assumed that the robot locomotes with the help of a prescribed trunk body and leg-tip trajectory in 3D Cartesian space. Also, it is assumed that the robot's body height varies in the 3D Cartesian space during locomotion, and a number of potential feet hold vertical positions across various terrains are identified between the foot and ground throughout the support phase. The overall set of explicitly constraint position equations that governs the system at any instant are first formed with respect to *G*

https://doi.org/10.1017/S0263574719001243 Published online by Cambridge University Press

and subsequently, transformed with respect to G_0 and is represented by the functions:

$$\mathbf{g}(\mathbf{p}^{G_0}) = 0 \ \in \mathbb{R}^{114} \tag{1}$$

The function $\mathbf{g}(\mathbf{p}^{G_0})$ has both kinematic joint constraints (n_c) as well as driving constraints. The vector of Cartesian coordinates is represented as follows:

$$\mathbf{p}^{G_0} = ((\mathbf{p}_0^{G_0})^T, (\mathbf{p}_1^{G_0})^T, (\mathbf{p}_2^{G_0})^T, (\mathbf{p}_3^{G_0})^T, (\mathbf{p}_4^{G_0})^T, (\mathbf{p}_5^{G_0})^T, (\mathbf{p}_6^{G_0})^T)^T \in \mathbb{R}^{114} \tag{2}$$

$$\mathbf{p}_i^{G_0} = ((\mathbf{p}_{i1}^{G_0})^T, (\mathbf{p}_{i2}^{G_0})^T, (\mathbf{p}_{i3}^{G_0})^T)^T \in \mathbb{R}^{18} \ (\boldsymbol{i} = \mathbf{1} - \mathbf{6}) \tag{3}$$

Here, the vectors of Cartesian coordinates of $\mathbf{P}_0$, $\mathbf{P}_{ij}$ with respect to $\boldsymbol{G}_0$ are represented by $\mathbf{p}_0^{G_0} = ((\mathbf{r}_{P_0O}^{G_0})^T, (\boldsymbol{\eta}_0)^T)^T \in \mathbb{R}^6$ and $\mathbf{p}_{ij}^{G_0} = ((\mathbf{r}_{P_{ij}O}^{G_0})^T, (\boldsymbol{\eta}_{ij})^T)^T \in \mathbb{R}^{108}$, respectively, where $\mathbf{r}_{P_0O}^{G_0} = \begin{bmatrix} x_{P_0O}^{G_0} & y_{P_0O}^{G_0} & z_{P_0O}^{G_0} \end{bmatrix}^T$ and $\mathbf{r}_{P_{ij}O}^{G_0} = \begin{bmatrix} x_{P_{ij}O}^{G_0} & y_{P_{ij}O}^{G_0} & z_{P_{ij}O}^{G_0} \end{bmatrix}^T$.

2.1.2. Inverse kinematics. The inverse kinematics analysis of the system that computes the joint displacement, velocity, and acceleration of the legs for a prescribed trunk body motion and swing leg-tip motion is essential, since it affects the dynamical control of the six-legged robotic system. The detailed calculations of the joint angles for such a walking six-legged robot are presented in *Mahapatra et al*.[45]

2.1.3. Terrain model. In the present study, the terrain along which the robot would maneuver varies from smooth to irregular topographies like flat, slope, banking, staircase, undulation, etc. The data points of the topology are predefined. The kinematics of the robotic system could be intimately connected to the represented terrain.

2.1.4. Trajectory and gait planning. Trajectory planning of a six-legged robot in various terrains is complex both from the point of view of computation and mechanisms (both swing and support phase) involved for accomplishment of a given task. The motion characteristics of the trunk body and tip of swing legs should be realistic and help to develop a robust inverse kinematics model. Therefore, the trunk body should have an uninterrupted and continuous motion for the given initial position, orientation (roll, pitch, and yaw), and maximum velocity of the trunk body. Similar characteristics also hold good for the swing leg as well. Hence, it is assumed that the motions are regulated by a step function that approximates the Heaviside step function with a cubic polynomial.[45]

Besides the effective trajectory planning, an effective gait planning and an efficient algorithm are also necessary to move the robot's legs in a sequential manner along straight, curved, transverse, spinning paths, etc. in various terrains. The kinematic outputs (displacement, velocity, acceleration, aggregate COM, etc.) are evaluated for a predefined 3D trunk body motion, swing leg trajectory planning of the feet-tip, and specified gait planning on various terrains. These outputs are subsequently transformed from reference frame $\boldsymbol{G}$ to frame $\boldsymbol{G}_0$, such that the velocity and acceleration vectors of the link ij with respect to $\boldsymbol{G}_0$ are represented by

$$\mathbf{v}_{ij}^{G_0} = ((\dot{\mathbf{r}}_{P_{ij}O}^{G_0})^T, ({}^{G_0}\boldsymbol{\omega}_{ij})^T)^T \in \mathbb{R}^{108}, \dot{\mathbf{v}}_{ij}^{G_0} = ((\ddot{\mathbf{r}}_{P_{ij}O}^{G_0})^T, ({}^{G_0}\dot{\boldsymbol{\omega}}_{ij})^T)^T \in \mathbb{R}^{108} \text{ where } i = 1{-}6, j = 1{-}3.$$

It is to be noted that force distribution and torque distribution depend both on gait parameters (e.g., straightforward, crab, turning gait, etc.) and on motion parameters (e.g., trunk body velocity, swing leg velocity, body height, lateral offset, crab angle, turning radius, etc.). So, in the present study, the kinematic outputs have been used to carry out dynamic analysis of the system for evaluating feet-forces and torques, etc.

2.2. Multi-body dynamic modeling of the six-legged robot

Dynamic modeling of the multi-legged robot system is complex, since such systems are characterized by many DOF, contact constraints or collision events, feet–ground interaction mechanics, and mass-moment of inertia settings. Also, for a multi-body system, complexities in the dynamical model arise due to the dynamic coupling caused by the kinematic constraints between each loop (like that formed by the support legs and the trunk body in a six-legged robotic system) and over-determinate input

https://doi.org/10.1017/S0263574719001243 Published online by Cambridge University Press

mechanisms. For real life robots, such dynamic models are required for the realistic simulation of legged system behaviors, thereby fine-tuning the gait parameters, geometrical design parameters, feedback control, etc. Now, to solve the dynamics of such systems, approaches like Lagrangian,[46,47] NE,[6] Gauss, and Kane[48] were adopted. In the present study, recursive NE approach is used to deal with the inverse dynamic or kinetostatic analysis of the robotic system and is expressed in over complete Cartesian coordinates ($\mathbf{p}^{G_0}$) in frame $\boldsymbol{G}_0$, such that

$$\mathbf{M}(\mathbf{p}^{G_0}) \cdot \dot{\mathbf{v}}^{G_0} = {}^{c}\mathbf{f} + \mathbf{f}(\mathbf{p}^{G_0}, \mathbf{v}^{G_0}) + \mathbf{q}_{GC}(\mathbf{p}^{G_0}, \mathbf{v}^{G_0}) \in \mathbb{R}^{114} \tag{4}$$

where $\mathbf{M}(\mathbf{p}^{G_0}) \in \mathbb{R}^{114}$ denotes the combined mass matrix of the robotic system; $\mathbf{v}^{G_0}$, $\dot{\mathbf{v}}^{G_0} \in \mathbb{R}^{24}$ denote the velocity and acceleration vector of the system, respectively, in Cartesian space; ${}^{c}\mathbf{f} \in \mathbb{R}^{114}$ represents the vector of reaction forces and joint torques associated with system coordinates; $\mathbf{f}\ (\mathbf{p}^{G_0}, \mathbf{v}^{G_0}) \in \mathbb{R}^{114}$ denotes the vector of both known and unknown applied forces and torques; $\mathbf{q}_{GC}(\mathbf{p}^{G_0}, \mathbf{v}^{G_0}) \in \mathbb{R}^{114}$ represents the vector of centrifugal forces and gyroscopic terms.

Eqs. (1) and (4) form a set of nonlinear equations commonly called the differential algebraic equations (DAE). This set of nonlinear equations governs the state of the robot in Cartesian space with respect to frame $\boldsymbol{G}_0$ at any instant of time.

Furthermore, the free-body diagram approach has been used for modelling the dynamics of the system. The NE equations are deduced for each of the isolated rigid bodies of the system and combined to form a set of equations of the system. But, handling such a large set of implicit constraint equations is computationally intensive. Hence, kinematic transformation technique has been implemented to reduce the set of 114 constraint equations expressed in Cartesian coordinates ($\mathbf{p}^{G_0}$) into 24 constraint equations in terms of generalized coordinates ($\mathbf{q}$). For detailed calculations, one can refer to Mahapatra *et al.* 2019.[42]

Furthermore, transformation of the inverse dynamic model (Eq. (4)) in terms of $\mathbf{q}$ has been realized with 24 numbers of equations. Out of 24 equations, first set of 6 equations defines dynamic behavior of the trunk body and payload (combined) at any instant of time with respect to the forces and moments such that,

$$\sum \mathbf{F}_i^{G_0} + \mathbf{F}_e^{G_0} = \mathbf{0}_3 \in \mathbb{R}^3 \tag{5}$$

$$\sum (\mathbf{s}_i^{G_0} \times \mathbf{F}_i^{G_0}) + \mathbf{M}_0^{G_0} + \mathbf{M}_e^{G_0} = \mathbf{0}_3 \in \mathbb{R}^3 \tag{6}$$

and the next set of 18 equations define the correlations between the joint torques, ground reaction forces, and moments on the legs, such that for leg i,

$$\mathbf{M}_i^{G_0} = -\mathbf{B}_i^{-1}\left(\mathbf{A}_i\mathbf{F}_i^{G_0} + \mathbf{D}_i\mathbf{T}_i^{G_0} + \mathbf{M}_{ei}^{G_0}\right) \in \mathbb{R}^{3} \tag{7}$$

where $\mathbf{M}_i^{G_0}$ denotes the vector of joint torques of leg i denoted by $[\, M_{i1}^{G_0}\ M_{i2}^{G_0}\ M_{i3}^{G_0}\,]^T$; $\mathbf{M}_{ei}^{G_0}$ denotes the vector representing the centrifugal, Coriolis, gyroscopic and gravitational moments acting on the leg i denoted by $[\, M_{ei1}^{G_0}\ M_{ei2}^{G_0}\ M_{ei3}^{G_0}\,]^T$; $\mathbf{B}_i = [1\ 0\ 0;\ 0\ 1\ 1;\ 0\ 0\ 1]^T$; $\mathbf{A}_i$ and $\mathbf{D}_i$ are the square matrices represented by $[a_{i1x}\ a_{i1y}\ a_{i1z}\ ;\ a_{i2x}\ a_{i2y}\ a_{i2z};\ a_{i3x}\ a_{i3y}\ a_{i3z}]^T$ and $[d_{i1x}\ d_{i1y}\ d_{i1z}\ ;\ d_{i2x}\ d_{i2y}\ d_{i2z};\ d_{i3x}\ d_{i3y}\ d_{i3z}]^T$, respectively; $\mathbf{s}_i^{G_0}$ is the displacement vector from point $\mathbf{P}_0$ to $\mathbf{P}_{i3}$ represented in reference frame $\boldsymbol{G}_0$; $\mathbf{M}_0^{G_0}$ is the vector of joint torques acting on the trunk body and payload (combined) denoted by $\left[\,0\ 0\ \sum_{i=1}^{6} M_{i1}^{G_0}\,\right]^T$; $\mathbf{F}_e^{G_0}$ and $\mathbf{M}_e^{G_0}$ are the vectors representing centrifugal, Coriolis, gyroscopic and gravitational forces and moments, respectively, acting on the combined mass of the trunk body and payload; $\mathbf{F}_i^{G_0}$ and $\mathbf{T}_i^{G_0}$ are the ground reaction force and moments at the foot of support leg i with respect to $\boldsymbol{G}_0$ denoted by vector $[\, F_{ix}^{G_0}\ F_{iy}^{G_0}\ F_{iz}^{G_0}\,]^T$ and $[\, T_{ix}^{G_0}\ T_{iy}^{G_0}\ T_{iz}^{G_0}\,]^T$, respectively, discussed in Section 2.3; $\mathbf{0}_3$ represents 3×1 zero matrix. For swing legs, $\mathbf{F}_i^{G_0} = \mathbf{0}_3$ and $\mathbf{T}_i^{G_0} = \mathbf{0}_3$. Furthermore, it is to be noted that Eq. (7) includes the moment of inertia terms of the robot body and legs, which again depend on the robot's geometry and shape of cross-section of the leg links.

https://doi.org/10.1017/S0263574719001243 Published online by Cambridge University Press

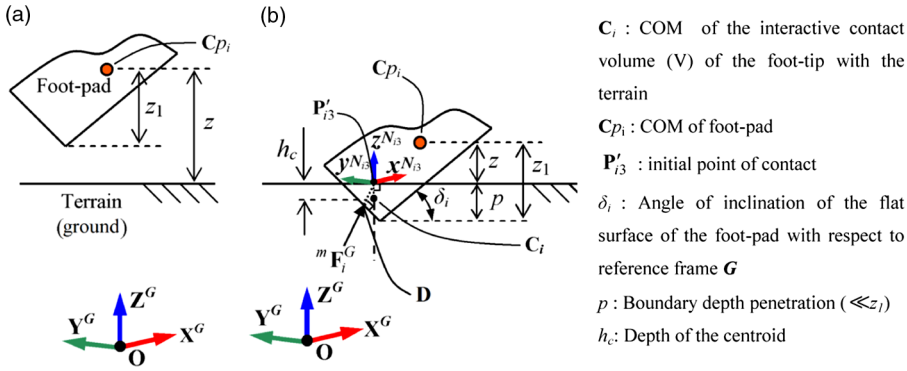

Fig. 2. Foot–ground contact (a) before impact and (b) after impact.

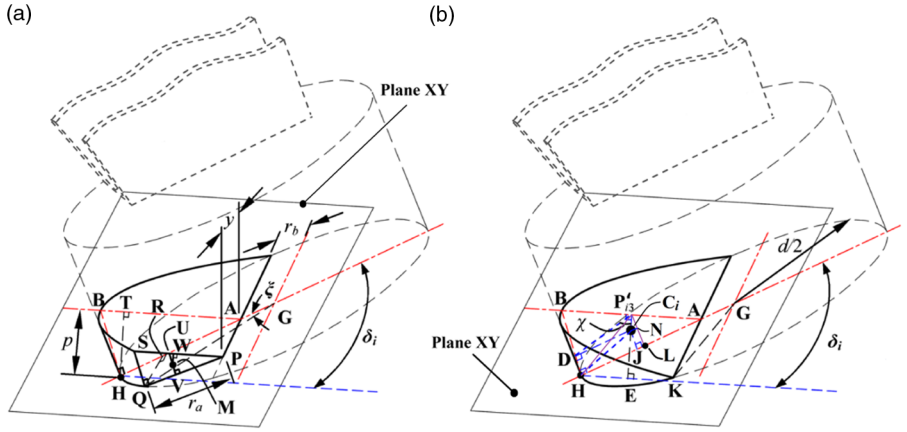

Fig. 3. Interactive contact volume between foot-pad and ground: (a) segmented volume, (b) total interaction volume.

2.3. Foot–ground interaction model

The foot–ground interaction mechanics model for the legged robots considered in the present study takes into account the compliance at the feet-tip with contact deformation and slip.[42] The model is developed based on deformable foot on hard terrain with a little deformation and defines the nonlinear interactive forces and moments according to viscoelastic compliant contact force and Amonton–Coulomb's friction law.

The foot-pad (assumed to be cylindrical in the present study) makes contact with the ground, when z becomes smaller than z_1 (refer to Fig. 2). Around the contact point, a small contact volume or interaction volume (V) is formed, which is subjected to compliance. The compliance at the interaction region between feet-tip and ground has a significant influence on the interaction mechanics. The foot-tip makes an oblique impact with the ground and a resultant impact force ${}^{m}\mathbf{F}_i^G$ is generated, which acts along the line $\mathbf{P}'_{i3\,\mathbf{D}}$, as shown in Fig. 2. Finally, the resultant ground reaction force at the foot of leg i with respect to $\boldsymbol{G}_0$ is given by,[42]

$$\mathbf{F}_i^{G_0} = \mathbf{A}^{G_0G}\mathbf{F}_i^G = \mathbf{A}^{G_0G}\mathbf{F}'^G_i + \mathbf{A}^{G_0G}\,{}^{m}\mathbf{F}_i^G \tag{8}$$

where $\mathbf{A}^{G_0G} \in \mathbb{R}^{3,3}$ is the transformation matrix that maps dynamic global reference frame ($\boldsymbol{G}$) into static global reference frame ($\boldsymbol{G}_0$); $\mathbf{F}_i^G$ is the net ground reaction force vector at the foot of support leg i with respect to $\boldsymbol{G}$; and $\mathbf{F}'^G_i$ is the resultant ground reaction force in the foot of leg i with respect to frame $\boldsymbol{G}$, when impact is zero during landing.

Now, to make the model more realistic, moment that acts on the foot due to interaction with the ground, denoted by $\mathbf{T}_i^{G_0}$, has been considered. This moment is approximated by the products of the resultant reaction force and their related arms. However, the interaction volume (V) has significant effect on the moment arm (line joining points $\mathbf{P}'_{i3}$ and H, as shown in Fig. 3). In the improved dynamic model carried out in the present study, trigonometrical relations have been used for calculation of the

https://doi.org/10.1017/S0263574719001243 Published online by Cambridge University Press

moment arm. To calculate that, at first, V is determined, which is followed by the determination of depth of the centroid ($\mathbf{C}_i$) denoted by h_c (refer to Fig. 2) for a boundary depth penetration (p). The z-axis of the local frame $\boldsymbol{N}_{i3}$ is perpendicular to the terrain surface, whereas y-axis is aligned with the longitudinal direction of the robot's body.

The point $\mathbf{C}_i$ lies on the plane ABH, as shown in Fig. 3(a), and is at a depth, h_c (COM of the contact volume) from the plane XY.

The following trigonometrical relationships are obtained from Fig. 3(a):

From ΔABH,

$$\mathrm{HA} = a = p/\sin\delta_i \tag{9}$$

$$\mathrm{HB} = b = p/\cos\delta_i \tag{10}$$

Again,

$$\delta_i = \pi/2 - (\beta_{i2} + \beta_{i3} - \psi) \tag{11}$$

and

$$\psi = \tan^{-1}\left(d\big/2l'_{i3}\right) \tag{12}$$

Here, p is the maximum depth of penetration; δ_i is the angle subtended by the bottom face of the foot-pad with the ground; β_{i2}, β_{i3} are the angular displacement of the joints; ψ is the bounding angle (refer to Mahapatra *et al.*[45]); d is the diameter of foot-pad; and l'_{i3} is the length of the tibia from the rotation axis to the circle center of foot-pad, that is, point $\boldsymbol{G}$.

Also,

$$\sin\delta_i = p\big/(d\big/2 - r_b) \tag{13}$$

where r_b is the distance from the chord of interception to the center of circle of the bottom face of the foot-pad.

Thus,

$$\mathrm{AG} = r_b = d\big/2 - p\big/\sin\delta_i \tag{14}$$

To calculate the total interaction volume (V), at first, the segmented volume is calculated. Let y be the perpendicular distance of the ΔPQS from the center of foot-pad, as shown in Fig. 3(a).

From ΔGRQ,

$$\cos\xi = \mathrm{RG/QG} = \sqrt{d^2 - 4y^2}\Big/d \tag{15}$$

Thus,

$$\mathrm{PQ} = r_a = \mathrm{QG}.\cos\xi - \mathrm{AG} = d/2.\cos\xi - r_b \tag{16}$$

By substituting Eq. (15) in Eq. (16), we get

$$\mathrm{PQ} = r_a = \frac{1}{2}\sqrt{d^2 - 4y^2} - r_b \tag{17}$$

and

$$\mathrm{SQ} = \mathrm{PQ}.\tan\delta_i = r_a.\tan\delta_i = \left(\frac{1}{2}\sqrt{d^2 - 4y^2} - r_b\right).\tan\delta_i \tag{18}$$

(Since ΔPQS and ΔABH are equivalent triangles, $\angle\mathrm{BHA} = \angle\mathrm{SQP} = \pi/2$ and $\angle\mathrm{BAH} = \angle\mathrm{SPQ} = \delta_i$.)

https://doi.org/10.1017/S0263574719001243 Published online by Cambridge University Press

From ΔAGK,

$$\mathrm{AK} = \sqrt{(d/2)^2 - r_b^2} \tag{19}$$

Area of the intercepted ΔPQS is given by:

$$A_y = 1/2.\ \mathrm{SQ.PQ} = \frac{1}{2}\mathrm{PQ}^2.\ \tan\delta_i = \frac{1}{2}r_a^2.\ \tan\delta_i \tag{20}$$

Therefore, interaction volume (V) of the interaction region is given by,

$$V = \oint dV = \int_{-AK}^{+AK} A_y dy = \int_{-AK}^{+AK} \frac{1}{2}r_a^2.\ \tan\delta_i .dy = \tan\delta_i .\ \int_0^{\sqrt{(d/2)^2 - r_b^2}} r_a^2.\ dy \tag{21}$$

Considering the segment ΔPQS in Fig 3(a), whose centroid is at M and the depth into the ground being the length WM (designated by h),

$$\mathrm{WM} = \mathrm{UM} \cdot \cos\delta_i = \frac{1}{3}\mathrm{SQ} \cdot \cos\delta_i \tag{22}$$

where $\angle\mathrm{UMW} = \delta_i$ and UM = UV-VM = $\frac{1}{3}$SQ for UV = $\frac{2}{3}$SQ, VM = $\frac{1}{3}$SQ.
By substituting Eq. (18) in Eq. (22), we get

$$\mathrm{WM} = \mathrm{r_a} \sin\delta_\mathrm{i}/3 \tag{23}$$

Therefore, the depth of COM of the contact volume (refer Figs. 2 and 3(b)) is given by,

$$\mathrm{P}'_{i3}\mathrm{C}_i = h_c = \oint \mathrm{WM} \cdot dV \Big/ \oint dV \tag{24}$$

By substituting Eqs. (21) and (23), in Eq. (24), we get

$$h_c = \sin\delta_i .\ \int_0^{\sqrt{(d/2)^2 - r_b^2}} r_a^3 \cdot dy \Big/ 3.\ \int_0^{\sqrt{(d/2)^2 - r_b^2}} r_a^2.\ dy \tag{25}$$

By substituting Eq. (17) in Eq. (25), we get

$$h_c = \frac{\sin\delta_i}{32}\left[\frac{3d^2(16r_b^2 + d^2)\cos^{-1}(2r_b/d) - 2r_b(8r_b^2 + 13d^2)\sqrt{d^2 - 4r_b^2}}{\left(d^2 + 2r_b^2\right)\sqrt{d^2 - 4r_b^2} - 3r_b d^2 \cos^{-1}\left(2r_b/d\right)}\right] \tag{26}$$

Similarly, support distance of the segment, ΔPQS is given by,

$$\mathrm{VP} = \frac{2}{3}r_a \tag{27}$$

For the entire contact volume,

$$\mathrm{JA} = r_e = \oint \mathrm{VP} \cdot dV \Big/ \oint dV \tag{28}$$

By substituting Eqs. (21) and (27) in Eq. (28), we get

$$r_e = 2.\ \int_0^{\sqrt{(d/2)^2 - r_b^2}} r_a^3 \cdot dy \Big/ 3.\ \int_0^{\sqrt{(d/2)^2 - r_b^2}} r_a^2.\ dy \tag{29}$$

By substituting Eq. (25) in Eq. (29), we get

$$r_e = 2h_c/\sin\delta_i \tag{30}$$

$$\mathrm{HJ} = \mathrm{DC}_i = d/2 - r_b - r_e \tag{31}$$

https://doi.org/10.1017/S0263574719001243 Published online by Cambridge University Press

From $\Delta \mathbf{DC}_i\mathbf{P}'_{i3}$,

$$\text{let } \angle \mathrm{DP}'_{i3}\mathrm{C}_i = \chi \tag{32}$$

From trigonometrical relationships,

$$\angle \mathrm{DC}_i\mathrm{P}'_{i3} = \pi/2 + \delta_i \tag{33}$$

From the laws of triangles,

$$\mathrm{P}'_{i3}\mathrm{D} = w = \sqrt{h_c^2 + (d/2 - r_b - r_e)^2 + 2h_c(d/2 - r_b - r_e)\sin\delta_i} \tag{34}$$

$$\cos\chi = \frac{\mathrm{P}'_{i3}\mathrm{D}^2 + \mathrm{P}'_{i3}\mathrm{C}_i^2 - \mathrm{DC}_i^2}{2\mathrm{P}'_{i3}\mathrm{D}\cdot\mathrm{P}'_{i3}\mathrm{C}_i} \tag{35}$$

and

$$\mathrm{P}'_{i3}\mathrm{D}^2 = \mathrm{P}'_{i3}\mathrm{C}_i^2 + \mathrm{DC}_i^2 + 2\mathrm{P}'_{i3}\mathrm{C}_i\cdot\mathrm{DC}_i\cdot\sin\delta_i \tag{36}$$

By substituting Eq. (36) in Eq. (35), we get

$$\chi = \cos^{-1}\left(\left(\mathrm{P}'_{i3}\mathrm{C}_i + \mathrm{DC}_i\cdot\sin\delta_i\right)/\mathrm{P}'_{i3}\mathrm{D}\right)\big) = \left(h_c + (d/2 - r_b - r_e)\cdot\sin\delta_i\right)/w \tag{37}$$

By applying the laws of triangles to $\Delta \mathrm{BD}^{\mathrm{P}'_{i3}}$, we have

$$\mathrm{BD} = \mathrm{P}'_{i3}\mathrm{D}\cdot\cos\chi\,/\cos\delta_i = w\cdot\cos\chi\,/\cos\delta_i \tag{38}$$

Hence,

$$\mathrm{HD} = \mathrm{HB} - \mathrm{BD} = (p - w\cdot\cos\chi)\,/\cos\delta_i \tag{39}$$

Again

$$\mathrm{HL} = \mathrm{HJ} + \mathrm{JL} = (d/2 - r_b - r_e) + h_c\sin\delta_i \tag{40}$$

$$\mathrm{P}'_{i3}\mathrm{L} = \mathrm{P}'_{i3}\mathrm{N} + \mathrm{NL} = h_c\cos\delta_i + (p - w\cdot\cos\chi)\,/\cos\delta_i\,(\because \mathrm{HD} = \mathrm{C}_i\mathrm{J} = \mathrm{NL}) \tag{41}$$

Therefore, moment arm is given by

$$\mathrm{HP}'_{i3} = \sqrt{\left(\mathrm{P}'_{i3}\mathrm{N}\right)^2 + (\mathrm{HL})^2} \tag{42}$$

By substituting Eqs. (40) and (41) in Eq. (42),

$$\mathrm{HP}'_{i3} = \sqrt{((d/2 - r_b - r_e) + h_c sin\delta_i)^2 + \left(h_c cos\delta_i + (p - w\cdot\cos\chi)\,/\cos\delta_i\right)^2} \tag{43}$$

Therefore, moments about a point **H** (refer to Fig 3(b)) with respect to frame $\boldsymbol{N}_{i3}$ is given by,

$$\vec{\mathbf{T}}_i^{N_{i3}} = \overrightarrow{\mathrm{HP}'_{i3}} \times \vec{\mathbf{F}}_i^{N_{i3}} = \vec{\mathbf{r}}_i^{N_{i3}} \times \vec{\mathbf{F}}_i^{N_{i3}} \tag{44}$$

$$\text{or } \mathbf{T}_i^{N_{i3}} = \tilde{\mathbf{r}}_i^{N_{i3}}\mathbf{F}_i^{N_{i3}} \tag{45}$$

where $\vec{\mathbf{r}}_i^{N_{i3}}$ is the displacement vector represented in frame $\boldsymbol{N}_{i3}$ from point P'_{i3} to **H;** $\tilde{\mathbf{r}}_i^{N_{i3}}$ is skew-symmetric matrix constructed from a displacement vector $\vec{\mathbf{r}}_i^{N_{i3}}$ in frame $\boldsymbol{N}_{i3}$.
Hence,

$$\mathbf{T}_i^G = \mathbf{A}^{GN_{i3}}\mathbf{T}_i^{N_{i3}} \tag{46}$$

and

$$\mathbf{T}_i^{G_0} = \mathbf{A}^{G_0G}\mathbf{T}_i^G = \mathbf{A}^{G_0G}\mathbf{A}^{GN_{i3}}\mathbf{T}_i^{N_{i3}} = \mathbf{A}^{G_0N_{i3}}\tilde{\mathbf{r}}_i^{N_{i3}}\mathbf{F}_i^{N_{i3}} \tag{47}$$

https://doi.org/10.1017/S0263574719001243 Published online by Cambridge University Press

where $\mathbf{A}^{GN_{i3}} \in \mathbb{R}^{3,3}$ is the transformation matrix that maps reference frame ($\boldsymbol{N}_{i3}$) into reference frame ($\boldsymbol{G}$); $\mathbf{A}^{G_0N_{i3}} \in \mathbb{R}^{3,3}$ is the transformation matrix that maps reference frame ($\boldsymbol{N}_{i3}$) into reference frame ($\boldsymbol{G}_0$).
Now,

$$\mathbf{F}_i^{N_{i3}} = \mathbf{A}^{N_{i3}G}\mathbf{F}_i^G \tag{48}$$

Since it is assumed that $\boldsymbol{G}$ and $\mathbf{N}_{i3}$ are parallel, we get

$$\mathbf{F}_i^{N_{i3}} = \mathbf{F}_i^G = \mathbf{A}^{GG_0}\mathbf{F}_i^{G_0} \tag{49}$$

By substituting Eqs. (8) and (49) in Eq. (47) gives, we get

$$\mathbf{T}_i^{G_0} = \mathbf{A}^{G_0N_{i3}}\tilde{\mathbf{r}}_i^{N_{i3}}\mathbf{F}_i^G = \mathbf{A}^{G_0N_{i3}}\tilde{\mathbf{r}}_i^{N_{i3}}A^{GG_0}\mathbf{F}_i^{G_0} \tag{50}$$

3. Feet-Forces' Optimization

In the present study, the inverse dynamic equilibrium Eq. (7) has many solutions corresponding to distribution of joint torques, feet-forces, and moments (54 unknowns). However, to find the best possible solution of the unknowns, the joint torques must meet the needs of the physical constraints, that is, both equality and inequality constraints. The constraints must be satisfied by each force distribution solution, no matter what method is adopted to obtain it. The problem now is to solve Eq. (7) using optimization techniques by introducing an objective function, namely minimization of the sum of the squares of joint torques.[49]
Mathematically, the objective function can be written as follows:

$$\text{Objective function: Minimize } S(\mathbf{T}^{G_0}) = \frac{1}{2}\left(\mathbf{M}^{G_0}\right)^T \mathbf{W}\mathbf{M}^{G_0} \tag{51}$$

where $\mathbf{W} \in \mathbb{R}^{18\times18}$ is a symmetric positive definite matrix,[6] and $M^{G_0}{}_{\in\mathbb{R}^{18}}$ is the overall joint torque vector. Eq. (51) involves quadratic optimization function, which means QP is to be applied. Now, minimization of the objective function is subjected to the following equality and inequality constraints.

(i) Forces and moments balance equations of the trunk body and payload
Refer to Eqs. (5) and (6)
(ii) Interactive forces and moments equations
Refer to Eqs. (8) and (50)
(iii) Ground frictional forces

$$\mathbf{Q}_i.\mathbf{A}^{GG_0}.\mathbf{F}_i^{G_0} \geq 0_4 \text{ (static friction, no slip condition)} \tag{52}$$

$$\mathbf{Q}_i.\mathbf{A}^{GG_0}.\mathbf{F}_i^{G_0} = 0_4 \text{ (dynamic friction, with slip condition)} \tag{53}$$

where $\mathbf{Q}_i$ is the friction coefficient matrix, as given by $Q_i = [-1\ 0\ \mu_{eff};\ 1\ 0\ \mu_{eff};\ 0\ -1\ \mu_{eff};\ 0\ 1\ \mu_{eff}]^T$. Here,$\mu_{eff}$ is kept equal to $\mu_s/\sqrt{2}$ for static friction and $\mu_d \Big/ \sqrt{2}$ for dynamic friction.[42]
(iv) Static equilibrium equation condition (conservation of moments)

$$\tilde{\mathbf{r}}_{C_mO}^{G_0}\mathbf{F}_{C_m}^{G_0} + \sum(\mathbf{T}_i^{G_0} + \tilde{\mathbf{r}}_{P_{i3}O}^{G_0}\mathbf{F}_i^{G_0}) = \mathbf{0}_3 \tag{54}$$

where $\tilde{\mathbf{r}}_{P_{i3}O}^{G_0}$ and $\tilde{\mathbf{r}}_{C_mO}^{G_0}$ are the skew symmetric matrices of the location vectors of the foot-tip in support phase and COM of the whole system, respectively, with respect to origin $\mathbf{O}$ in frame $\boldsymbol{G}_0$; $\mathbf{F}_{C_m}^{G_0}$ is the vector of gravitational forces acting on the system denoted by $[0\ 0\ \left(m_0 + \sum_{i=1}^{6}\sum_{j=1}^{3} mij\right) g]^T$. The terms "$T_i^{G_0} + \tilde{r}_{P_{i3}O}^{G_0}F_i^{G_0}$" is the external moment that describes how the ground is reacting to the six-legged robot's motion with respect to base-frame origin $\boldsymbol{G}_0$. For more details, one may refer to Mahapatra *et al.* 2019.[42]

https://doi.org/10.1017/S0263574719001243 Published online by Cambridge University Press

(v) Actuator torque limitation constraints (physical limits of actuator torques)
In the present study, authors have tried to find out the optimal force and torque distributions, so that the required joint torque does not exceed the actuator's capacity to navigate through the sloping terrain, staircase, and others. Therefore,

$$M_{ij,\min} \leq M_{ij}^{G_0} \leq M_{ij,\max} \text{ for } I = 1-6, j = 1-3 \tag{55}$$

where $M_{ij}^{G_0}$ is the torque at the j^{th} joint of i^{th} leg, and $M_{ij,min}$ and $M_{ij,max}$ are the torque limits at the j^{th} joint of i^{th} leg, which are generally decided based on the motor specifications.
The function can be further expressed in terms of primary variables (F^{G_0}), to compute the optimal feet-forces as described in the following section.

3.1. Objective function in terms of F^{G_0}

The overall joint torque vector is represented by

$$\mathbf{M}^{G_0} = \left[(\mathbf{M}_1^{G_0})^T \ (\mathbf{M}_2^{G_0})^T \ (\mathbf{M}_3^{G_0})^T \ (\mathbf{M}_4^{G_0})^T \ (\mathbf{M}_5^{G_0})^T \ (\mathbf{M}_6^{G_0})^T \right] \in \mathbb{R}^{18} \tag{56}$$

Furthermore, $M_i^{G_0}$ (I = 1–6) is the torque vector of each joint and is the function of primary variables, which, in this case, are the foot forces $F_{ix}^{G_0}$, $F_{iy}^{G_0}$, and $F_{iz}^{G_0}$. It is obtained by substituting (50) in (7) such that,

$$\mathbf{M}_i^{G_0} = -\mathbf{B}_i^{-1} \left(\mathbf{A}_i \mathbf{F}_i^{G_0} + \mathbf{D}_i \mathbf{T}_i^{G_0} + \mathbf{M}_{ei}^{G_0} \right) = \mathbf{U}_i \mathbf{F}_i^{G_0} + \mathbf{V}_i \tag{57}$$

where

$$\mathbf{T}_i^{G_0} = \mathbf{A}^{G_0 N_{i3}} \tilde{\mathbf{r}}_i^{N_{i3}} \mathbf{A}^{G G_0} \mathbf{F}_i^{G_0} \in \mathbb{R}^3 \tag{58}$$

$$\mathbf{U}_i = -\mathbf{B}_i^{-1} \left(\mathbf{A}_i + \mathbf{D}_i \mathbf{A}^{G_0 N_{i3}} \tilde{\mathbf{r}}_i^{N_{i3}} \mathbf{A}^{G G_0} \right) \in \mathbb{R}^{3\times 3} \tag{59}$$

$$\mathbf{V}_i = -\mathbf{B}_i^{-1} \mathbf{M}_{ei}^{G_0} \in \mathbb{R}^3 \tag{60}$$

Likewise, the overall joint torque vector is denoted by

$$\mathbf{M}^{G_0} = \mathbf{U}\mathbf{F}^{G_0} + \mathbf{V} \tag{61}$$

where

$$\mathbf{U} = \begin{bmatrix} \mathbf{U}_1 & \mathbf{0}_3 & \dots & \mathbf{0}_3 \\ \mathbf{0}_3 & \mathbf{U}_2 & \dots & \mathbf{0}_3 \\ \vdots & \vdots & \ddots & \vdots \\ \mathbf{0}_3 & \mathbf{0}_3 & \dots & \mathbf{U}_6 \end{bmatrix} \in \mathbb{R}^{18\times 18} \tag{62}$$

$$\mathbf{F}^{G_0} = \left[(\mathbf{F}_1^{G_0})^T \ (\mathbf{F}_2^{G_0})^T \ (\mathbf{F}_3^{G_0})^T \ (\mathbf{F}_4^{G_0})^T \ (\mathbf{F}_5^{G_0})^T \ (\mathbf{F}_6^{G_0})^T \right] \in \mathbb{R}^{18} \tag{63}$$

$$\mathbf{V} = \begin{bmatrix} \mathbf{V}_1^T & \mathbf{V}_2^T & \mathbf{V}_3^T & \mathbf{V}_4^T & \mathbf{V}_5^T & \mathbf{V}_6^T \end{bmatrix} \in \mathbb{R}^{18} \tag{64}$$

Now, substituting (61) in (51), the objective function can be written as follows:

$$\begin{aligned} S(\mathbf{T}^{G_0}) &= \frac{1}{2} \left(\mathbf{U}\mathbf{F}^{G_0} + \mathbf{V} \right)^T \mathbf{W} \left(\mathbf{U}\mathbf{F}^{G_0} + \mathbf{V} \right) \\ &= \frac{1}{2} \left(\mathbf{F}^{G_0} \right)^T \bar{\mathbf{H}} \mathbf{F}^{G_0} + \mathbf{c}^T \mathbf{F}^{G_0} + \frac{1}{2} \mathbf{V}^T \mathbf{W} \mathbf{V} \end{aligned} \tag{65}$$

where $\bar{\mathrm{H}}_{\in \mathbb{R}^{18\times 18}}$ is an auxiliary variable called the Hessian matrix. It is a Jacobian square matrix that includes the coefficients of all the quadratic terms of the objective function. **W** is a symmetric matrix.

https://doi.org/10.1017/S0263574719001243 Published online by Cambridge University Press

$\mathbf{c}_{\in\mathbb{R}^{18}}$ is also an auxiliary variable, such that

$$\overline{\mathbf{H}} = \mathbf{U}^T \mathbf{W} \mathbf{U} \tag{66}$$

$$\mathbf{c} = \mathbf{U}^T \mathbf{W} \mathbf{V} \tag{67}$$

The last term of (65) does not depend on F^{G_0}. So, the new objective function can be described by a new equation,

$$S(\mathbf{F}^{G_0}) = \frac{1}{2} \left(\mathbf{F}^{G_0}\right)^T \bar{\mathbf{H}} \mathbf{F}^{G_0} + \mathbf{c}^T \mathbf{F}^{G_0} \tag{68}$$

Now, equation (68) is subjected to some equality and inequality constraints, which are discussed in the following sections.

3.2. Force-moment equality constraints

Eq. (54) in matrix form is written as follows:

$$\tilde{\mathbf{r}}^{G_0}_{C_m O} \mathbf{F}^{G_0}_{C_m} + \sum (\mathbf{T}^{G_0}_i + \tilde{\mathbf{s}}^{G_0}_i \mathbf{F}^{G_0}_i) = \mathbf{0}_3 \tag{69}$$

Substituting Eq. (58) in Eq. (69) and rearranging,

$$\sum \mathbf{K}_i \mathbf{F}^{G_0}_i = -\tilde{\mathbf{r}}^{G_0}_{C_m O} \mathbf{F}^{G_0}_{C_m} \tag{70}$$

where

$$\mathbf{K}_i = \mathbf{A}^{G_0 N_{i3}} \tilde{\mathbf{r}}^{N_{i3}}_i \mathbf{A}^{G G_0} + \tilde{\mathbf{s}}^{G_0}_i \in \mathbb{R}^3 \tag{71}$$

By rearranging, we get

$$\mathbf{K} \mathbf{F}^{G_0} = -\tilde{\mathbf{r}}^{G_0}_{C_m O} \mathbf{F}^{G_0}_{C_m} \tag{72}$$

where

$$\mathbf{K} = \left[\tilde{\mathbf{K}}_1 \ \tilde{\mathbf{K}}_2 \ \tilde{\mathbf{K}}_3 \ \tilde{\mathbf{K}}_4 \ \tilde{\mathbf{K}}_5 \ \tilde{\mathbf{K}}_6 \right] \in \mathbb{R}^{3\times 18} \tag{73}$$

By rearranging (5), we get

$$\mathbf{I}_0 \mathbf{F}^{G_0} = -\mathbf{F}^{G_0}_e \tag{74}$$

where

$$\mathbf{I}_0 = \left[\mathbf{I}_3 \ \mathbf{I}_3 \ \mathbf{I}_3 \ \mathbf{I}_3 \ \mathbf{I}_3 \ \mathbf{I}_3 \right] \in \mathbb{R}^{3\times 18} \tag{75}$$

$\mathbf{I}_3$ is an identity matrix.
Similarly, Eq. (6) reduces to

$$\mathbf{R} \mathbf{F}^{G_0} = -\mathbf{M}^{G_0}_0 - \mathbf{M}^{G_0}_e \tag{76}$$

where

$$\mathbf{R} = \left[\tilde{\mathbf{s}}^{G_0}_1 \ \tilde{\mathbf{s}}^{G_0}_2 \ \tilde{\mathbf{s}}^{G_0}_3 \ \tilde{\mathbf{s}}^{G_0}_4 \ \tilde{\mathbf{s}}^{G_0}_5 \ \tilde{\mathbf{s}}^{G_0}_6 \right] \in \mathbb{R}^{3\times 18} \tag{77}$$

By combining equality constraints (72), (74), and (76), the overall set of equality constraints is given by:

$$\mathbf{A}_e \cdot \mathbf{F}^{G_0} = \mathbf{B}_e \tag{78}$$

$$\text{where } \mathbf{A}_e = \left(\mathbf{K};\ \mathbf{I}_0;\ \mathbf{R}\right)^T, \in \mathbb{R}^{9\times 18} \tag{79}$$

$$\mathbf{B}_e = -\left(\tilde{\mathbf{r}}^{G_0}_{C_m O} \mathbf{F}^{G_0}_{C_m};\ \mathbf{F}^{G_0}_e;\ \mathbf{M}^{G_0}_0 + \mathbf{M}^{G_0}_e \right)^T \in \mathbb{R}^9 \tag{80}$$

https://doi.org/10.1017/S0263574719001243 Published online by Cambridge University Press

3.3. Joint torque inequality constraints
For each joint, by using Eq. (55), we have

$$M_{ij,\min} \leq M_{ij}^{G_0} \leq M_{ij,\max} \tag{81}$$

For each leg i,

$$\begin{pmatrix} M_{i1,\min} \\ M_{i2,\min} \\ M_{i3,\min} \end{pmatrix} \leq \begin{pmatrix} M_{i1}^{G_0} \\ M_{i2}^{G_0} \\ M_{i3}^{G_0} \end{pmatrix} \leq \begin{pmatrix} M_{i1,\max} \\ M_{i2,\max} \\ M_{i3,\max} \end{pmatrix} \tag{82}$$

$$\mathbf{M}_{i,\min} \leq \mathbf{M}_i^{G_0} \leq \mathbf{M}_{i,\max} \in \mathbb{R}^3 \tag{83}$$

For all the legs,

$$\mathbf{M}_{\min} \leq \mathbf{M}^{G_0} \leq \mathbf{M}_{\max} \in \mathbb{R}^{18} \tag{84}$$

By substituting Eq. (20) in Eq. (43),

$$\mathbf{M}_{\min} \leq \mathbf{U}\mathbf{F}^{G_0} + \mathbf{V} \leq \mathbf{M}_{\max} \tag{85}$$

which means,

$$\mathbf{U}\mathbf{F}^{G_0} \geq \mathbf{M}_{\min} - \mathbf{V} \tag{86}$$

and

$$-\mathbf{U}\mathbf{F}^{G_0} \geq \mathbf{V} - \mathbf{M}_{\max} \tag{87}$$

3.4. Friction force inequality constraints
By combining (52) and (53),

$$\mathbf{Q}_i \mathbf{A}^{GG_0} \mathbf{F}_i^{G_0} \geq \mathbf{0}_4 \tag{88}$$

Therefore, composite friction force inequality constraints for all the legs can be written as follows:

$$\mathbf{Q}\mathbf{F}^{G_0} \geq \mathbf{0}_{24} \tag{89}$$

$$\text{where } \mathbf{Q} = \begin{bmatrix} \mathbf{Q}_1.\mathbf{A}^{GG_0} & \mathbf{0}_3 & \dots & \mathbf{0}_3 \\ \mathbf{0}_3 & \mathbf{Q}_2.\mathbf{A}^{GG_0} & \dots & \mathbf{0}_3 \\ \vdots & \vdots & \ddots & \vdots \\ \mathbf{0}_3 & \mathbf{0}_3 & \dots & \mathbf{Q}_6.\mathbf{A}^{GG_0} \end{bmatrix} \in \mathbb{R}^{24\times 18} \tag{90}$$

By combining Eqs. (86), (87), and (89), the overall set of inequality constraints is given by:

$$\mathbf{A}_u \cdot \mathbf{F}^{G_0} \geq \mathbf{B}_u \tag{91}$$

$$\text{where } \mathbf{A}_u = \left(\mathbf{U};\ -\mathbf{U};\ \mathbf{Q}\right)^T \in \mathbb{R}^{60\times 18} \tag{92}$$

$$\mathbf{B}_u = \left(\mathbf{M}_{\min} - \mathbf{V};\ \mathbf{V} - \mathbf{M}_{\max};\ \mathbf{0}_{24}\right)^T \in \mathbb{R}^{60} \tag{93}$$

Therefore, in standard QP form, the optimization problem can be written as follows:

$$\min_{\mathbf{F}^{G_0}} : S(\mathbf{F}^{G_0}) = \frac{1}{2}\left(\mathbf{F}^{G_0}\right)^T \tilde{\mathbf{H}}\mathbf{F}^{G_0} + \mathbf{c}^T\mathbf{F}^{G_0} \tag{94}$$

subject to

$$\mathbf{A}_e \cdot \mathbf{F}^{G_0} = \mathbf{B}_e \tag{95}$$

$$\mathbf{A}_u \cdot \mathbf{F}^{G_0} \geq \mathbf{B}_u. \tag{96}$$

https://doi.org/10.1017/S0263574719001243 Published online by Cambridge University Press

Hence, the coupled dynamical system is mathematically expressed as a constrained optimization problem and solved in MATLAB using QP approach to determine the finite ranges of feet-forces and torque distributions in all the legs, which are considered to be appropriate according to the criteria described by the Eqs. (95) and (96).

4. Simulations, Experiment, and Validation

In the present study, numerical simulation and experiments are carried out to confirm the validity of the proposed algorithm. The environment and robot model as described in Section 2.1 are kept the same both in case of simulations using VP tools and experiments. Two case studies of the six-legged robot locomotion in various terrains with alternating tripod gait (DF = 1/2) are carried out in the below subsections to determine the accuracy of the developed algorithm. In the first case, rigid multi-body dynamical analysis is carried out analytically by simulating in MATLAB and validated using VP tools. The second case study is undertaken to compare the experimental results with the analytical and simulated results of MSC.ADAMS®.

The VP involved the following important steps: (1) development of the CAD model of the six-legged robot using solid modeler CATIA V5, (2) defining the joints and contacts in CATIA Simdesigner Workbench, (3) exporting as a MSC.ADAMS® compatible file format, (4) preprocessing, execution, and postprocessing of the analysis results in MSC.ADAMS®. The physical and contact parameters are given in Table I. The contact parameter values (refer to Table I) supplied as inputs to the proposed model are basically the default input values used by MSC.ADAMS® to solve the contact problems.

4.1. Case I: Staircase climbing

In the present case study, maneuverability of the realistic six-legged robot climbing up a staircase (breadth, $b_s = 0.25$ m; height, $h_s = 0.05$ m) has been analyzed. The kinematic analysis of the system is performed with predefined input parameters using MATLAB solver, and thereafter, multi-body dynamic analysis of the system has been carried out with the motion inputs obtained from the study of kinematics.

The frames $\boldsymbol{G}_0$ and $\boldsymbol{G}$ are assumed to be parallel and coincide at origin **O,** that is, $\boldsymbol{\eta}_G = (0, 0, 0)^T$. The robot's trunk body remained parallel to the slope of staircase at any instant of time. Therefore, initial position and orientation of $\mathbf{P}_0$ with respect to global frame $\boldsymbol{G}$ is given by $\boldsymbol{p}_0^G = \{0, 0.412, 0.235, \tan^{-1}(h_s/b_s), 0, 0\}^T$. The corresponding initial joint angles are calculated from the CAD model and taken in the order of $[\theta_{i1}, \beta_{i2}, \beta_{i3}]$ (for I = 1–6), so that these angles become equal to [5°, −16°, −69°] for leg 1, [12°,16°, 69°] for leg 2, [12°, −16°, −69°] for leg 3, [18.5°,16°, 69°] for leg 4, [22°, −16°, −69°] for leg 5, and [27.5°,16°, 69°] for leg 6. The initial velocity of the trunk body moving parallel to the slope is assumed to be equal to $v_{yz} = 0.1$ m/s. The maximum swing height of each leg along $\boldsymbol{Z}$ with respect to local frame of reference ($\boldsymbol{L}_{i3}$) attached to leg-tip at $\mathbf{P}_{i3}$ (start point of swing) becomes equal to $\mathrm{Hm}_{in} + \Delta h = 0.072$ m, where Hm_{in} is the maximum height of the terrain on the path of swing leg i in the n^{th} duty cycle, Δh is the additional clearance between the terrain and swing height Hm_{in}.[45] The value of landing height with respect to frame $\boldsymbol{L}_{i3}$, at the instant, when the leg comes to support is assumed to be equal to $h'_{in} = h_s = 0.05$ m. The maximum slip velocity (v_f) is assumed to be equal to 0.001 m/s with a slip angle $\varepsilon_s = 45°$. The simulation is carried out in MATLAB for three duty cycles ($n = 3$) with time step $h = 0.05$ s and trunk body's stroke length (s_0) of 0.125 m.

The elapsed time for three duty cycles is computed as 8.6 s with the time period of first, second, and third cycles as 3.0, 2.6, and 3.0 s respectively. The computed kinematic motion parameters (displacement, velocity, acceleration, etc.) based on the motion and gait planning algorithms are provided as necessary inputs to the inverse dynamics model. Besides these parameters, the physical and contact parameters defined in Table I are also given as inputs. Additionally, the actuator torque is limited to ±6 Nm for computation of optimal feet-forces, joint torques, etc. The optimization algorithm chosen is `interior-point-convex quadprog` that satisfies the boundary conditions at each iteration corresponding to the objective function. Subsequently, to validate the analytical model using VP tools, the 3D CAD model is preprocessed in CATIA SimDesigner and imported into MSC.ADAMS®, so that relevant inputs like joint angular velocities (results obtained analytically), contact parameters of the interacting surface, etc. can be defined for the CAD model before execution. In the present case, MSC.ADAMS® solver used a default *gear stiff* (GSTIFF) *integrator* (backward differentiation formulation) algorithm to solve the DAEs of the dynamic problem. Here,

https://doi.org/10.1017/S0263574719001243 Published online by Cambridge University Press

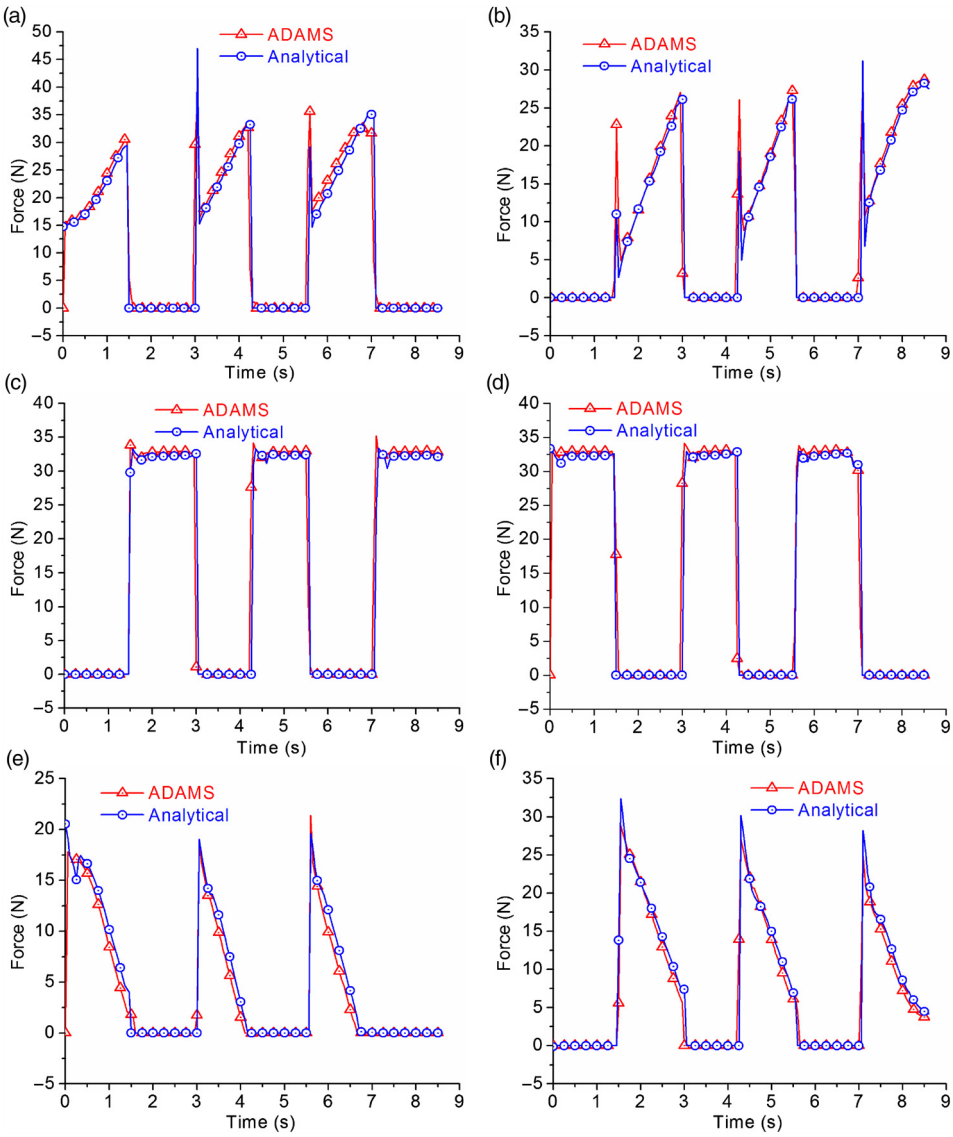

Fig. 4. Normal contact force distribution on the leg-tips of the six-legged robot with respect to frame $\boldsymbol{G}_0$ while ascending a staircase with tripod gait: (a) Leg1, (b) Leg2, (c) Leg3, (d) Leg4, (e) Leg5, (f) Leg6.

the time interval of 0.05 s is kept the same as that obtained analytically for developing the simulation of the system. The computed results like the optimal force distribution in the legs, joint torques, and power consumptions obtained by using (a) analytical method and (b) MSC.ADAMS® are analyzed over three gait cycles keeping the total cycle time same. The results are in close agreement which proves the efficacy of the developed algorithm.

Figure 4 shows the optimal distributions of feet-forces ($\mathbf{F}_i^{G_0}$) in all the legs of the six-legged robot plotted against time interval of $h = 0.05$ s.

For the wave gait strategy with DF = 1/2, the support and swing phase times are kept equal for all the legs. It has followed a wave sequence like, (1) legs 1-4-5 in support phase and legs 2-3-6 in swing phase; (2) legs 2-3-6 in support phase and legs 1-4-5 in swing phase. The graphs revealed that the pattern of the normal reaction foot force ($F_{iz}^{G_0}$) experienced by the legs 1-2, 3-4, and 5-6 are similar except that the pattern is out of phase by 180°. This might be attributed to the fact that wave gaits are regular and symmetric, with the right and left legs of each column having a phase difference of a half-cycle. Also, it is seen that when a leg is in swing motion, the forces in that leg is zero and is denoted by straight line. When the robot climbs upstairs, the entire COG of the system moves forward. This could be well explained by the graph, since the normal feet-forces on the front legs in support phase increase, while that on the rear legs decrease with time till the start of next swing

https://doi.org/10.1017/S0263574719001243 Published online by Cambridge University Press

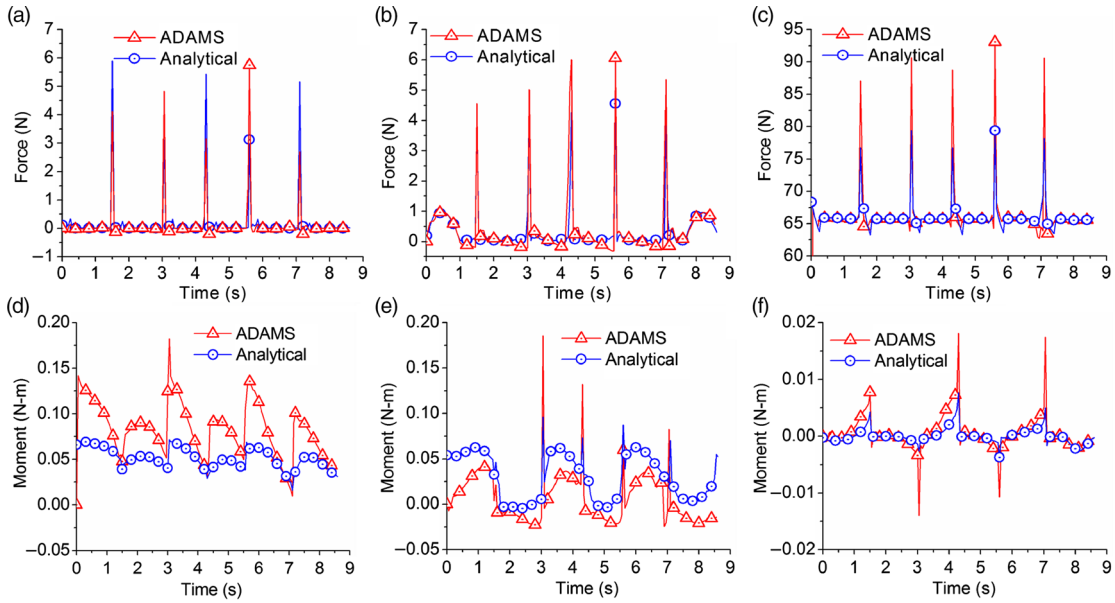

Fig. 5. Summation of forces and moments distribution with respect to frame $\boldsymbol{G}_0$: (a) ΣF_{ix}, (b) ΣF_{iy}, (c) ΣF_{iz}, (d) ΣT_{ix}, (e) ΣT_{iy}, (f) ΣT_{iz}, where I = 1–6.

phase. Moreover, the variations of normal force distributions in the middle legs (refer to Fig. 4(c) and (d)) are found to be less and the values are approximately constant. This could be attributed to the fact that the foothold positions of the legs during support phase are close to the COG of the system.

It is also interesting to note that summation of all the normal reaction feet-forces at any instant of time with respect to $\boldsymbol{G}_0$ balances the weight of the six-legged robot with payload (i.e., 65.7 N) except during impact, which is assumed to last for the fraction of a second (refer to Fig. 5(c)). A momentary impulsive force is generated, when the leg-tip collides with the ground at the start of support phase. There is a sudden shoot in the normal reaction foot force $F_{iz}^{G_0}$, as can be well observed from Fig. 5(c). It is also important to mention that the horizontal components of forces ($F_{ix}^{G_0}$ and $F_{iy}^{G_0}$) do exist, although their magnitude is not significant enough (Fig. 5(a) and (b)). Similarly, it is observed that the moment of forces acting at the foot-tip of a support leg (refer to Fig. 5(d) and (e)) are insignificant and kept within the average range of $+0.4$ to -0.01 Nm (MATLAB) excluding the sudden shoots due to impact.

Figure 6 shows the torque distributions in all the joints of the legs. It is observed that the torques values during support phases are significantly higher compared to that during swing phase for each leg. Also, the torque experienced by joint $i2$ of each leg is the higher compared to that experienced by the other two joints at any instant of time during support phase. Moreover, torque variations in the middle legs are less compared to that of the front and rear legs (refer to Fig. 6(c) and (d)) since the location of the joints of these legs are close to the COG of the system. It is also interesting to note that the impact force (sudden high shoot out as shown in Fig. 6) experienced by any leg when it touches the ground has significant effect on the joint torques (sudden high shoot out as shown in Fig. 6) of its own leg and considerable effect on the joints of other legs. Figure 7 shows the snapshots of the simulations carried out in MSC.ADAMS® of a realistic six-legged robot climbing a staircase. From the motion of the robot, it is evident that the system is stable and follows a desired tripod gait sequence of 1-4-5 and 2-3-6.

4.2. Case II: Experimentation with a real six-legged robot maneuvering on a concrete floor

Experiment is carried out with a commercial Hexcrawler HDATS Robot and the supported infrastructure available. An attempt has been made to correlate the normal foot forces' distribution of a real six-legged robot with the simulated ones of a realistic one without any payload. To stay as closely as possible to the reality, simulation environment is kept the same, as it would be executed on real robot. The experimental results are compared with that of analytical ones of the proposed model executed in MATLAB and that obtained by solving in MSC.ADAMS® subjected to the same initial inputs for all the three modes of measurement.

https://doi.org/10.1017/S0263574719001243 Published online by Cambridge University Press

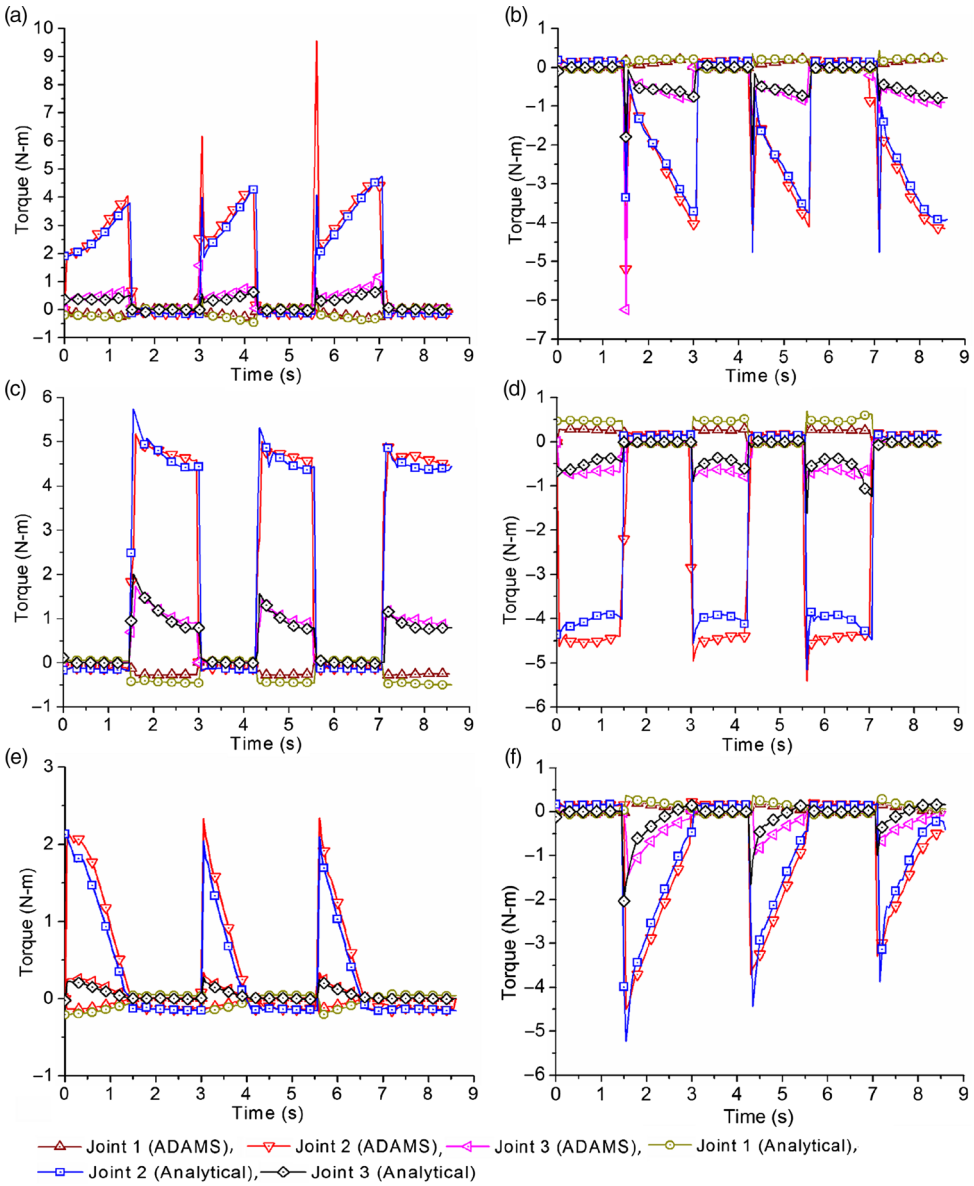

Fig. 6. Torque distribution in various joints of the six-legged robot while ascending a staircase with tripod gait: (a) Leg, (b) Leg2, (c) Leg3, (d) Leg4, (e) Leg5, (f) Leg6.

The robot moved on a flat concrete floor with straightforward motion. The objective is to obtain normal feet-forces' distributions data in all the six legs. The experiment is conducted using a complete program installed on the robot that could give command to it to perform straight forward motion with DF = 1/2, trunk body stroke length (s_0) of 0.085 m, and trunk body velocity of 0.075 m/s. The experiment is said to be completed after three duty cycles (n = 3). To measure the feet-forces, the head ends of the piezoresistive flexiforce sensors (six in numbers) are attached to the foot-pad of each leg (refer to Fig. 8), while the conductive leads at the tail end are attached to a flexiforce adapter circuit (filter cum amplifier circuit) for obtaining steady noise-free force data. Each of the adapters are connected to an Arduino UNO board (refer to Fig. 6), which is further connected to a remote computer through com-port for real-time data acquisition. The data are filtered in MATLAB for further processing. It is to be noted that the calibration of each of the sensor is a must and has been carried out using standard force measuring gauge. Furthermore, using three degree polynomial curve fit, a relationship is obtained between the sensor reading and actual reading.

Simulation is carried out for the developed inverse dynamic model in MATLAB for three duty cycles with the total time of analysis computed as 8.16 s (1st cycle: 2.88 s; 2nd cycle: 2.4 s; 3rd cycle: 2.88 s) and time step (h) of 0.08 s. Similarly, computation is performed in MSC.ADAMS® solver

https://doi.org/10.1017/S0263574719001243 Published online by Cambridge University Press

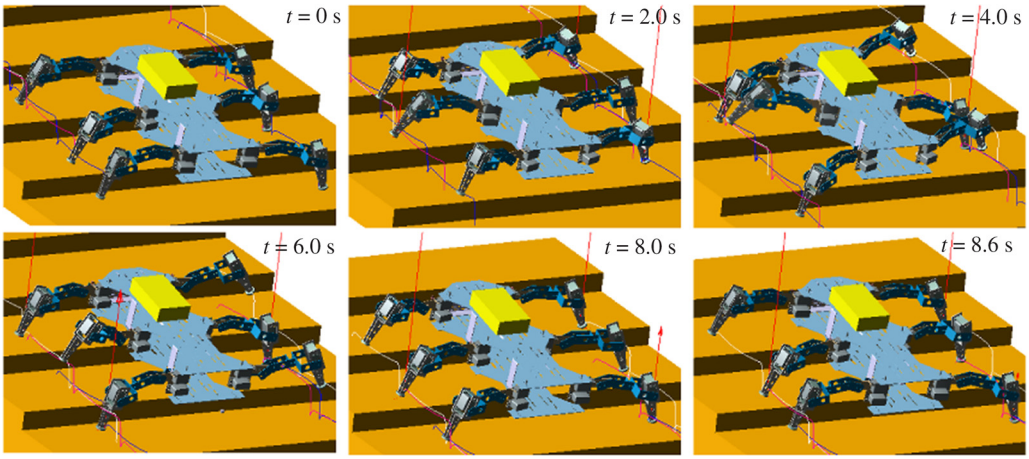

Fig. 7. Snapshots of a realistic six-legged robot simulated in MSC.ADAMS® while climbing a staircase with tripod gait.

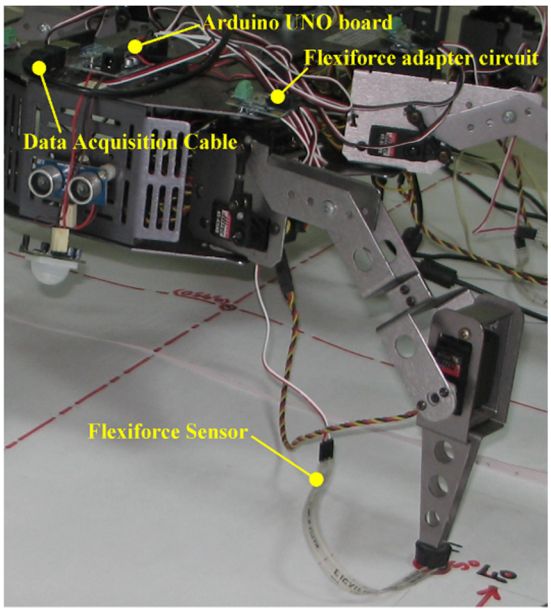

Fig. 8. Experimental set-up of a real six-legged robot (Hexcrawler HDATS) showing the data acquisition system.

using the CAD model keeping all the conditions similar. The experimental data for the distribution of normal feet-forces are compared with the analytical and simulated data for over three duty cycles with respect to $\boldsymbol{G}_0$, as shown in Fig. 9. Looking at the plotted graphs of the normal feet-forces' distribution in the different legs obtained by various methods (experiment, analytical, and MSC.ADAMS®), it can be inferred that the distribution trends are similar and in close agreement. It is also noticeable that though the developed mathematical model and the MSC.ADAMS® model of the realistic six-legged robot could generate an impact force instantaneously at the beginning of contact of feet tip with the ground during support phase, no such impact force is observed during experiment. The reason for such behavior might be due to the fact that flexiforce sensors are not sensitive enough to sense the impact, which is in the range of milliseconds.

A comparative study of the summation of normal contact forces, which should be equivalent to the weight of the six-legged robot is illustrated in Fig. 10. At any instant, the experimental value is less compared to the computed ones. Moreover, it is also observed that for the three cycles, the total sum of forces obtained experimentally varies in the range of 20.0–23.5 N (approximately), while computationally the range is found to be from 24 to 25 N (approximately). Such variations in the experimental data are clearly due to the different portions of the area of leg-tip of the Hexcrawler coming in contact with the ground during support phase, the most effective being at the time when the value of ϑ_{i1} becomes close to zero. This means that at every instant, the flexiforce sensor must

https://doi.org/10.1017/S0263574719001243 Published online by Cambridge University Press

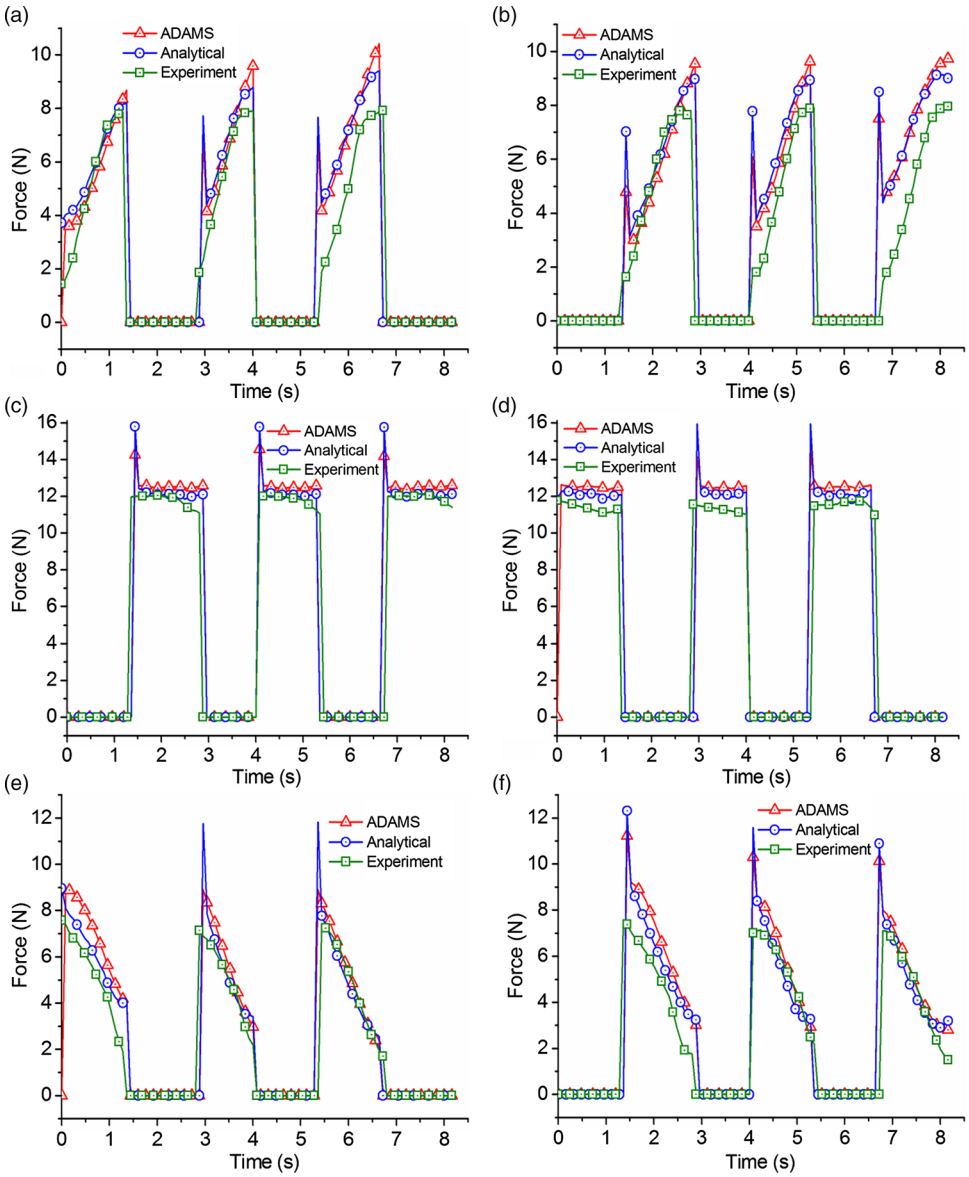

Fig. 9. Comparative study of the normal contact force distribution on the leg-tips of the six-legged robot with respect to frame $\boldsymbol{G}_0$ moving on a concrete floor with tripod gait: (a) Leg1, (b) Leg2, (c) Leg3, (d) Leg4, (e) Leg5, (f) Leg6.

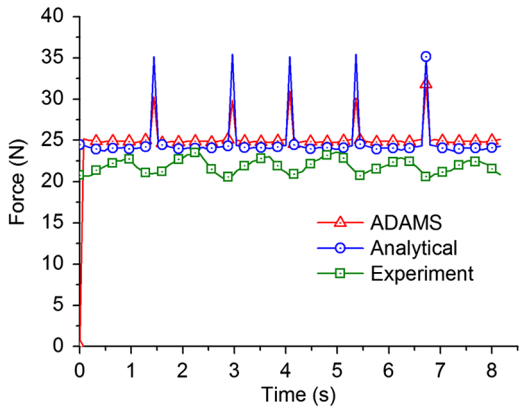

Fig. 10. Summation of the normal contact force distribution, $F_{iz}(I = 1–6)$ with respect to frame $\boldsymbol{G}_0$.

https://doi.org/10.1017/S0263574719001243 Published online by Cambridge University Press

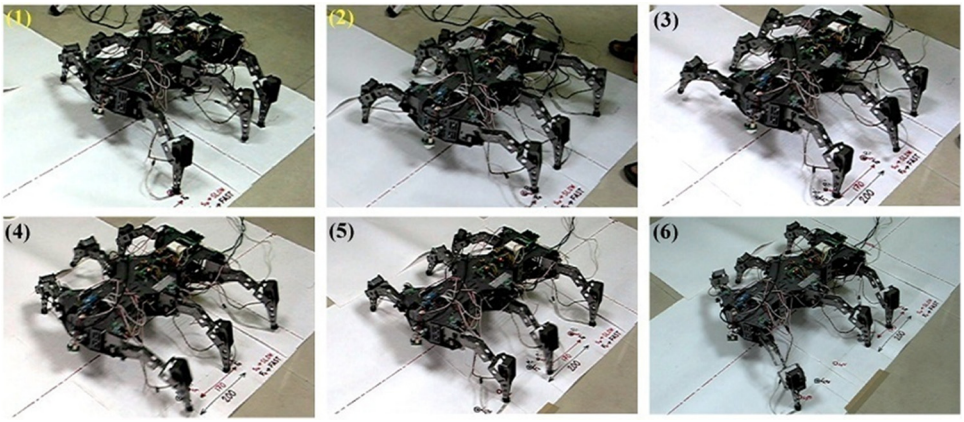

Fig. 11. Snapshots of a real six-legged robot (Hexcrawler HDATS) moving on a concrete floor with tripod wave gait.

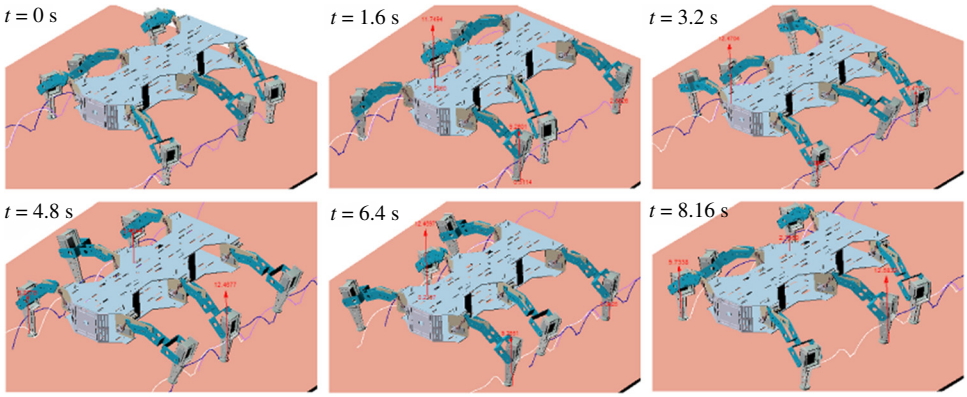

Fig. 12. Snapshots of a realistic six-legged robot simulated in MSC.ADAMS® moving on a concrete floor with tripod gait.

be adjusted, so that it comes into adequate ground contact, which is somewhat difficult with such type of sensor configuration. Such sensors should be customized to adapt the geometrical shape of the pad in contact with the ground, which is beyond the scope of the present work. However, overall, the validation proves the efficacy of the proposed model with respect to the trend followed by the normal force distribution.

Snapshots of the experimental (refer to Fig. 11) and simulated (refer to Fig. 12) data in MSC.ADAMS® show that the motion of the robot is stable and in accordance with the desired tripod gait sequence of 1-4-5 and 2-3-6.

5. Conclusions and Scopes for Future Work

This study proposes a new analytical coupled dynamics model with compliant contact impact and slip of the leg-tips of a six-legged robot consisting of interconnected rigid multi-bodies. Such investigation has not been addressed before. A large number of kinematic constraint equations of the coupled system are effectively handled by the use of kinematic transformation algorithms for efficient computation. The validation carried out with the help of numerical solvers like MSC.ADAMS® and experimental tests conducted under different conditions have confirmed the effectiveness of the proposed algorithm. Furthermore, the analytical model with formulation of the quadratic optimization function as minimization of the sum of the squares of joint torques, subject to equality and inequality constraints with compliant contact and friction model, provides efficient distribution of feet-forces in the legs during support phase, such that they are in close agreement with the simulated data. The experimental data of normal feet-forces' distribution marginally deviate from the analytical data, which may be attributed to the fact that sufficient contact during support phase is not there due to sensor configuration. More sensitive sensors can be mounted to measure the feet–ground interaction forces and verify the dynamic model of the robot, but it is beyond the scope of the present study.

https://doi.org/10.1017/S0263574719001243 Published online by Cambridge University Press

The compliant normal impact function has worked well as a method for calculating the normal force during collision of leg-tip with the ground. It is found from the analytical data that as a leg touches the ground, impact force is generated (sudden shoots), whose effect is also observed in the joint torques of its own leg and that of others due to coupling effects. Moreover, it is observed that the middle revolute joint of each leg experiences more torque compared to the other joints. It is also important to notice that the torques in joints of all the legs are more during support phase compared to that of the swing phase, which is obvious since the weight of the trunk body and payload are transferred to the ground through these support legs. The total horizontal components of feet-forces' distribution and the moment of forces acting at the foot-tip of a support leg are not significant enough during the locomotion of the robot except during impact when sudden shoots are observed. The validation, thereby, paves the way for further design iterations with the proposed algorithm, aiming to find optimal distribution of the feet-forces, moments, and joint torques, which will help to develop energy efficient power consumption model for six-legged robots under various surface conditions and different gait strategies in the future work. Future work will also focus on the development of active force control algorithms for real-time implementation in six-legged robotic systems. This modeling technique can be extended further in future to tackle the problems related to dynamic reactions with perturbations.

Acknowledgments

The first author is thankful to Kondalarao Bhavanibhatla, M.Tech, NIT Durgapur and Kaustav Biswas, B.Tech, NIT Durgapur for their help. He is also thankful to the Director, CSIR-CMERI, Durgapur for rendering all sorts of cooperation for conducting the research work.

References

1. H. Wang, L. Sang, X. Hu, D. Zhang and H. Yu, "Kinematics and dynamics analysis of a quadruped walking robot with parallel leg mechanism," *Chinese J. Mech. Eng*. **26**(5), 881–891 (2013).
2. X. Y. Sandoval-Castro, M. Garcia-Murillo, L. A. Perez-Resendiz and E. Castillo-Castañeda, "Kinematics of Hex-Piderix - A six-legged robot - Using screw theory," *Int. J. Adv. Robot. Sys*. **10**(19), 1–8 (2013).
3. S. S. Roy, A. K. Singh and D. K. Pratihar, "Estimation of optimal feet forces and joint torques for on-line control of six-legged robot," *Robot. Comput. Integr. Manuf*. **27**(5), 910–917 (2011).
4. B. Jin, C. Chen and W. Li, "Power consumption optimization for a hexapod walking robot," *J. Intell. Robot. Syst*. **71**(2), 195–209 (2013).
5. P. G. de Santos, E. Garcia, R. Ponticelli and M. Armada, "Minimizing energy consumption in hexapod robots," *Adv. Robot*. **23**(6), 681–704 (2009).
6. M. S. Erden and K. Leblebicioglu, "Torque distribution in a six-legged robot," *IEEE Trans. Robot*. **23**(1), 179–186 (2007).
7. S. S. Roy and D. K. Pratihar, "Effects of turning gait parameters on energy consumption and stability of a six-legged walking robot," *Robot. Auto. Sys*. **60**(1), 72–82 (2012).
8. U. Saranli and M. Buehler, "Modeling and analysis of a spatial compliant hexapod," *Technical papers,* Department of Electrical Engineering and Computer Science, McGill University, Montreal, Canada (1999) pp. 1–18.
9. A. S. Yigit, A. P. Christoforou and M. A. Majeed, "A nonlinear visco-elastoplastic impact model and the coefficient of restitution," *Nonlin. Dynam*. **66**(4), 509–521 (2011).
10. I. Han and B. J. Gilmore, "Multi-body impact motion with friction- analysis, simulation and experimental validation," *ASME J. Mech. Des*. **115**(3), 412–422 (1993).
11. P. Bergés and A. Bowling, "Rebound, slip, and compliance in the modeling and analysis of discrete impacts in legged," *J. Vib. Control* **12**(12), 1407–1430 (2006).
12. J. P. Schmiedeler and K. J. Waldron, "Impact analysis as a design tool for the legs of mobile robots," **In:** *Advances in Robot Kinematics* (J. Lenarcic and M. M. Stanisic eds.) (Kluwer Academic Publishers, Norwell, MA, 2000) pp. 129–136.
13. L. Jingtao, W. Feng, Y. Huangying, W. Tianmiao and Y. Peijiang, "Energy efficiency analysis of quadruped robot with trot gait and combined cycloid foot trajectory," *Chinese J. Mech. Eng.* **27**(1), 138–145 (2014).
14. D. M. Gorinevsky and A. Y. Shneider, "Force control in locomotion of legged vehicles over rigid and soft surfaces," *Int. J. Robot. Res*. **9**(2), 4–23 (1990).
15. J.-S. Chen, F.-T. Cheng, K.-T. Yang, F.-C. Kung and S. York-Yih, "Optimal force distribution in multilegged vehicles," *Robotica* **17**(2), 159–172 (1999).
16. S. S. Roy and D. K. Pratihar, "Kinematics, dynamics and power consumption analyses for turning motion of a six-legged robot," *J. Intell. Robot. Syst.* **74**(3–4), 663–688 (2014).
17. M. Machado, P. Moreira, P. Flores and H. M. Lankarani, "Compliant contact force models in multibody dynamics: Evolution of the Hertz contact theory," *Mech. Mach. Theory* **53**, 99–121 (2012).
18. J. A. C. Ambrósio, "Impact of Rigid and Flexible Multibody Systems: Deformation Description and Contact Models," **In:** *Virtual Nonlinear Multibody Systems, NATO ASI Series* (W. Schiehlen and M. Valasek eds.) (Springer Science and Business Media, Dordrecht, 2003) pp. 57–81. doi:10.1007/978-94-010-0203-5.

19. S.-S. Bi, X.-D. Zhou and D. B. Marghitu, "Impact modelling and analysis of the compliant legged robots," *Proc. Inst. Mech. Eng. Part K J. Multi-body Dyn*. **226**(2), 85–94 (2012).
20. M. M. Gor, P. M. Pathak, A. K. Samantaray, J.-M. Yang and S. W. Kwak, "Control oriented model-based simulation and experimental studies on a compliant legged quadruped robot," *Robot. Auto. Syst*. **72**, 217–234 (2015).
21. S. R. Hamner, A. Seth, K. M. Steele and S. L. Delp, "A rolling constraint reproduces ground reaction forces and moments in dynamic simulations of walking, running, and crouch gait," *J. Biomech*. **46**(10), 1772–1776 (2013).
22. G. Gilardi and I. Sharf, "Literature survey of contact dynamics modeling," *Mech. Mach. Theory* **37**(10), 1213–1239 (2002).
23. R. Brach, *Mechanical Impact Dynamics: Rigid Body Collisions* (Brach Engineering, LLC, Naperville, IL, 2007).
24. K. Hunt and F. Crossley, "Coefficient of restitution interpreted as damping in vibroimpact," *Trans. ASME J. Appl. Mech*. **42**, 440–445 (1975).
25. D. W. Marhefka and D. E. Orin, "A compliant contact model with nonlinear damping for simulation of robotic systems," *IEEE Trans. Syst. Man Cybern. Part A Syst. Hum.* **29**, 566–572 (1999).
26. L. Ding, H. Gao, Z. Deng, J. Song, Y. Liu, G. Liu and K. Iagnemma, "Foot–terrain interaction mechanics for legged robots: Modeling and experimental validation," *Int. J. Robot. Res*. **32**(13), 1585–1606 (2013).
27. V. Vasilopoulos, I. S. Paraskevas and E. G. Papadopoulos, "Compliant Terrain Legged Locomotion Using a Viscoplastic Approach," *IEEE/RSJ International Conference on Intelligent Robots and Systems (IROS'14),* Chicago, Illinois, USA (2014) pp. 4849–4854.
28. T. W. Lee and A. C. Wang, "On the dynamics of intermittent-motion mechanisms—Part 1: Dynamic model and response," *J. Mech. Trans. Auto. Des*. **105**(3), 534–540 (1983).
29. Q. Bombled and O. Verlinden, "Dynamic simulation of six-legged robots with a focus on joint friction," *Multibody Syst. Dyn*. **28**(4), 395–417 (2012).
30. M. Azad and R. Featherstone, "A new nonlinear model of contact normal force," *IEEE Trans. Robot*. **30**(3), 736–739 (2014).
31. R. Kikuuwe, N. Takesue, A. Sano, H. Mochiyama and H. Fujimoto, "Fixed-Step Friction Simulation: From Classical Coulomb Model to Modern Continuous Models," *Proceedings of IEEE/RSJ International Conference on Intelligent Robots and Systems*, Edmonton, Canada (2005) pp. 3910–3917.
32. M. Rajaei and H. Ahmadian, "Development of generalized Iwan model to simulate frictional contacts with variable normal loads," *Appl. Math. Model*. **38**(15–16), 4006–4018 (2014).
33. D. E. Orin and Y. Oh, "Control of force distribution in robotic mechanisms containing closed kinematic chains," *ASME J. Dyn. Syst. Meas. Control* **102**, 134–141 (1981).
34. J. Kerr and A. Roth, "Analysis of multifingered hands," *Int. J. Robot. Res*. **4**(4), 3–17 (1986).
35. F.-T. Cheng and D. E. Orin, "Efficient algorithm for optimal force distribution—the compact-dual LP method," *IEEE Trans. Robot. Auto*. **6**(2), 178–187 (1990).
36. D. C. Kar, K. K. Issac and K. Jayarajan, "Minimum energy force distribution for a walking robot," *J. Robot. Syst.* **18**(2), 47–54 (2001).
37. Z. Li, S. S. Ge and S. Liu, "Contact-force distribution optimization and control for quadruped robots using both gradient and adaptive neural networks," *IEEE Trans. Neural Netw. Learn. Syst*. **25**(8), 1460–1473 (2014).
38. A. Jiang, M. Liu and D. Howard, "Optimization of legged robot locomotion by control of foot-force distribution," *Trans. Inst. W.Y. Meas. Control* **26**(4), 311–323 (2004).
39. A. Bowling, "Dynamic performance, mobility, and agility of multilegged robots," *ASME J. Dyn. Syst. Meas. Control* **128**(4), 765–777 (2006).
40. V. Kumar and K. J. Waldron, "Force distribution in walking vehicles," *ASME J. Mech. Des*. **112**(1), 90–99 (1990).
41. F. B. Ouezdou, O. Bruneau and J. C. Guinot, "Dynamic analysis tool for legged robots," *Multibody Syst. Dyn*. **2**(4), 369–391 (1998).
42. A. Mahapatra, S. S. Roy and D. K. Pratihar, "Study on feet forces' distributions, energy consumption and dynamic stability measure of hexapod robot during crab walking," *Appl. Math. Model*. **65**, 717–744 (2019).
43. X. Ding and F. Yang, "Study on hexapod robot manipulation using legs," *Robotica* **34**(2), 468–481 (2016).
44. H. Hahn, *Rigid Body Dynamics of Mechanisms 1- Theoretical Basis*, 1st edn. (Springer, Berlin, 2002).
45. A. Mahapatra, S. S. Roy and D. K. Pratihar, "Computer aided modeling and analysis of turning motion of hexapod robot on varying terrains," *Int. J. Mech. Mater Des*. **11**(3), 309–336 (2015).
46. A. Dumlu and K. Erenturk, "Modeling and trajectory tracking control of 6-DOF RSS type parallel manipulator," *Robotica* **32**(4), 643–657 (2014).
47. Y. Daud, A. A. Mamun and Jian-Xin Xu, "Dynamic modeling and characteristics analysis of lateral-pendulum unicycle robot," *Robotica* **35**(3), 537–568 (2017).
48. P. Wu, H. Xiong and J. Kong, "Dynamic analysis of 6-SPS parallel mechanism," *Int. J. Mech. Mater. Des.* **8**(2), 121–128 (2012).
49. E. F. Fukushima and S. Hirose, "Attitude and Steering Control of the Long Articulated Body Mobile Robot KORYU," **In:** *Climbing and Walking Robots, Towards New Applications* (H. Zhang ed.) (Itech Education and Publishing, Vienna, Austria, 2007) pp. 23–48.